The Astrophysical Journal, 832:210 (21pp), 2016 December 1 doi:10.3847/0004-637X/832/2/210

THE CARNEGIE-CHICAGO HUBBLE PROGRAM. I. AN INDEPENDENT APPROACH TO THE EXTRAGALACTIC DISTANCE SCALE USING ONLY POPULATION II DISTANCE INDICATORS*

Rachael L. Beaton[1], Wendy L. Freedman[2], Barry F. Madore[1], Giuseppe Bono[3,4], Erika K. Carlson[1], Gisella Clementini[5], Meredith J. Durbin[6], Alessia Garofalo[5,7], Dylan Hatt[2], In Sung Jang[8], Juna A. Kollmeier[1], Myung Gyoon Lee[8], Andrew J. Monson[9], Jeffrey A. Rich[1], Victoria Scowcroft[1], Mark Seibert[1], Laura Sturch[1], and Soung-Chul Yang[10]

[1] The Observatories of the Carnegie Institution for Science, 813 Santa Barbara Street, Pasadena, CA 91101, USA; rbeaton@obs.carnegiescience.edu
[2] Department of Astronomy & Astrophysics, University of Chicago, 5640 South Ellis Avenue, Chicago, IL 60637, USA
[3] Dipartimento di Fisica, Universitá di Roma Tor Vergata via Della Ricerca Scientifica 1, I-00133, Roma, Italy
[4] INAF-Osservatorio Astronomico di Roma, Via Frascati 33, I-00040 Monte Porzio Catone, Italy
[5] INAF-Osservatorio Astronomico di Bologna, via Ranzani 1, I-40127, Bologna, Italy
[6] Space Telescope Science Institute, 3700 San Martin Drive, Baltimore, MD 21218, USA
[7] Dipartimento di Fisica e Astronomia, Universitá di Bologna, Viale Berti Pichat 6/2, I-40127 Bologna, Italy
[8] Department of Physics & Astronomy, Seoul National University, Gwanak-gu, Seoul 151-742, Korea
[9] Department of Astronomy & Astrophysics, The Pennsylvania State University, 525 Davey Lab, University Park, PA 16802, USA
[10] Korea Astronomy and Space Science Institute (KASI), Daejeon 305-348, Korea
Received 2016 June 6; revised 2016 August 30; accepted 2016 September 30; published 2016 December 1

ABSTRACT

We present an overview of the Carnegie-Chicago Hubble Program, an ongoing program to obtain a 3% measurement of the Hubble constant (H_0) using alternative methods to the traditional Cepheid distance scale. We aim to establish a completely independent route to H_0 using RR Lyrae variables, the tip of the red giant branch (TRGB), and Type Ia supernovae (SNe Ia). This alternative distance ladder can be applied to galaxies of any Hubble type, of any inclination, and, using old stars in low-density environments, is robust to the degenerate effects of metallicity and interstellar extinction. Given the relatively small number of SNe Ia host galaxies with independently measured distances, these properties provide a great systematic advantage in the measurement of H_0 via the distance ladder. Initially, the accuracy of our value of H_0 will be set by the five Galactic RR Lyrae calibrators with *Hubble Space Telescope* Fine-Guidance Sensor parallaxes. With *Gaia*, both the RR Lyrae zero-point and TRGB method will be independently calibrated, the former with at least an order of magnitude more calibrators and the latter directly through parallax measurement of tip red giants. As the first end-to-end "distance ladder" completely independent of both Cepheid variables and the Large Magellanic Cloud, this path to H_0 will allow for the high-precision comparison at each rung of the traditional distance ladder that is necessary to understand tensions between this and other routes to H_0.

Key words: cosmological parameters – distance scale – stars: Population II – stars: variables: RR Lyrae

1. INTRODUCTION

The determination of cosmological parameters has improved dramatically over the past two decades. The "factor-of-two" controversy over the value of the Hubble constant was resolved at the turn of the century (Freedman et al. 2001), and only a decade later, quoted precisions are being claimed at the 3%–5% level (e.g., Riess et al. 2011, 2016; Freedman et al. 2012b), not only for H_0, but also for many of the other fundamental cosmological parameters. With measurements from the *Wilkinson Microwave Anisotropy Probe* (*WMAP*), the *Hubble Space Telescope* (*HST*) H_0 Key Project, large-scale surveys of Type I supernovae (SNe Ia)—including the *Supernovae, H_0, for the Equation of State of Dark Energy* (*SH$_0$ES*; e.g., Riess & Macri 2007; Riess et al. 2011, 2016), and the *Carnegie Supernova Project* (CSP; e.g., Freedman et al. 2009; Folatelli et al. 2010), as well as from baryon acoustic oscillations made from the ground (BAO; e.g., Eisenstein et al. 2005; Anderson et al. 2014), and most recently, cosmic microwave background (CMB) modeling with *Planck* (e.g., Planck Collaboration et al. 2011, 2015) a standard cosmological model has emerged. This "Concordance Model" (e.g., Spergel et al. 2007; Komatsu et al. 2011) was challenging to envision at the outset of the H_0 Key Project (Freedman et al. 2001), when there existed 10σ discrepancies in measurements of H_0 for relatively small samples of nearby galaxies (Saha et al. 2001). At that time, the different programs differed by up to a factor of two in their estimates, although each quoted errors of only 10% on their own measurement (see, e.g., Table 6 in Sandage et al. 2006, for a summary of the literature at that time).

Today the situation is qualitatively quite different. The local determinations of H_0, using a progressively constructed "distance ladder," traditionally anchored on Cepheid variables, consistently give a value of the Hubble constant around 74 ± 3 km s^{-1} Mpc^{-1} (Riess et al. 2011, 2016; Freedman et al. 2012b). On the other hand, H_0 can be estimated from a fit to the measured power spectrum of CMB anisotropies to infer the local expansion rate of the universe (Planck Collaboration et al. 2014, 2015). The CMB value of H_0, extracted from the modeled data, is 67.3 ± 1.2 km s^{-1} Mpc^{-1}. Figure 1 presents recent measurements of H_0 limited to those derived from either

* Based on observations made with the NASA/ESA *Hubble Space Telescope*, obtained at the Space Telescope Science Institute, which is operated by the Association of Universities for Research in Astronomy, Inc., under NASA contract NAS 5-26555. These observations are associated with programs #13472 and #13691.

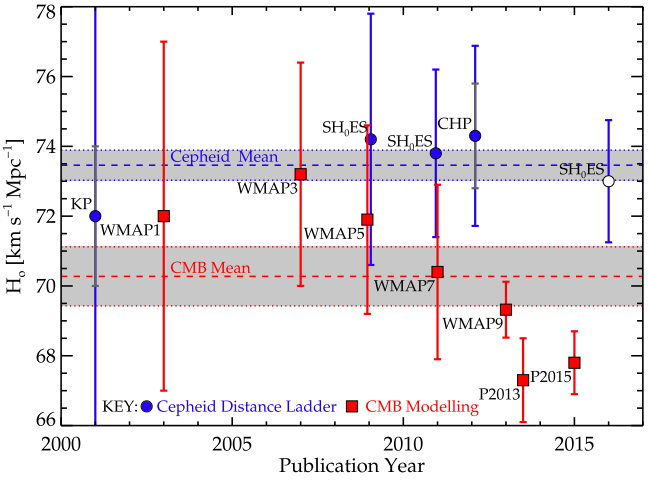

Figure 1. Comparison of recent determinations of H_0 using the Cepheid distance ladder (blue circles) and CMB modeling techniques (red squares) as a function of publication year, with the recent value from Riess et al. (2016) given as an open circle. Many of the projects shown here have multiple measurements, but effort was taken to choose the measurements that are most comparable; for the Cepheid distance ladder the "preferred value" based on the different anchors is used and for the CMB modeling values are shown using similar input priors on cosmological parameters (see Table 1 for a more exhaustive list of individual and best-estimate values). Colored error bars represent the "total" error (quadrature sum of random and systematic) quoted at the time of publication, with the gray error bars indicating just the random component (but only if it was indicated in the publication; see Table 1). The 1σ range of the mean for the Cepheid distance ladder and CMB modeling are shown as the shaded regions with the mean indicated by a dashed line. These two approaches, which use techniques that are "local" and "cosmological" in nature, respectively, differ by more than 3σ in their unweighted mean values. As demonstrated here, the tension has grown with the accumulating CMB data sets.

the distance ladder ("local")[11] or the CMB anisotropies ("cosmological").[12]

Figure 1 demonstrates that the "local" and "cosmological" solutions are more than 3σ apart. While the distance ladder H_0 measurements are consistent even for multiple groups, the value of H_0 inferred from cosmological modeling, in contrast, has monotonically decreased with the acquisition of progressively better CMB maps (in resolution, sensitivity, and spectral coverage). Once again, an accurate determination of the expansion rate of the universe comes down to an intercomparison of the stated error bars on the results of two competing methods of measuring H_0—a situation similar to that motivating the *HST* H_0 Key Project twenty years ago (Freedman et al. 2001).

The broad agreement between H_0 derived from the distance ladder and from cosmological models is actually quite impressive given the very different methodologies being employed. However, the value of the Hubble constant applies so much leverage to the covariantly dependent solutions of other cosmological parameters (simultaneously embedded in the CMB data) that it remains crucial to determine if there is new physics or simply as-yet-unappreciated systematics driving these differences.

1.1. Uncertainties in Current H_0 Measurements

We turn now to a discussion of the uncertainties in both the distance ladder and CMB methods for determining H_0. A longstanding "first rung" for the distance ladder is the Large Magellanic Cloud (LMC). The distance to the LMC is, in itself, a source of active research (see, for instance, the summary of de Grijs et al. 2014), and its suitability as the "anchor" for the distance ladder is much debated (see, for instance, Efstathiou 2014). The LMC is a low-metallicity, dwarf irregular galaxy, unlike the spiral galaxies with higher metallicity and higher luminosity that are common hosts to SNe Ia. The potential for metallicity effects between their Cepheid populations is therefore a concern. The proximity of the LMC to the Sun permits the application of numerous independent distance measurement techniques, however, including those with uncertainties much easier to control than those of the Cepheids. Of note is the work of Pietrzyński et al. (2013), in which a set of eight late-type double-eclipsing binaries in the LMC were used to obtain a (largely geometric) 2.2% estimate of the distance to the LMC. On the other hand, the proximity of the LMC also means that its three-dimensional structure and line-of-sight depth are both of larger concern than in most extragalactic applications, and extra attention must be given to membership in specific structural components for a given distance tracer (for further discussion, see Clementini et al. 2003; Clementini 2011; Moretti et al. 2014). Replacement of the LMC with the megamaser-host NGC 4258 as the anchor point for the distance ladder provides an independent zero-point calibration, but does not fully settle the issue of the zero-point, given that, effectively, only one data set exists (with multiple distinct distance measurements, including Herrnstein et al. 1999; Humphreys et al. 2013; Riess et al. 2016, among others), for which the systematic errors are difficult to ascertain.

The advantages of the Leavitt law (or the Cepheid period–luminosity (PL) relation[13]) are well known. (a) Cepheids are intrinsically high-luminosity supergiants. (b) In the infrared, especially, their PL relations have small intrinsic dispersion (~0.1 mag) for the *I* band and redder wavelengths. (c) They are found in all star-forming galaxies (spiral and irregular). Lastly, (d) their variability is sufficiently stable over a human lifetime that they can be repeatedly observed with different instruments operating at different wavelengths and thereby be tested for any number of systematic effects. Transient objects (like SNe Ia) are much more problematic in the latter regard. There are remaining challenges for the Cepheid distance ladder, however, such as (a) the need for a robust determination of the metallicity dependence of the Leavitt law, particularly at optical wavelengths (e.g., Romaniello et al. 2005, 2008, among

[11] For visual simplicity, we have limited this to just those papers providing an end-to-end distance ladder measurement.

[12] Figure 1 uses the "preferred" H_0 results from specific works, which often combine different anchor points for the Leavitt Law. We note, however, that while the difference in the distance to the LMC adopted between the KP and the most recent *SH$_0$ES* determination is <0.1%, thereby comparisons between those measurements, despite the dramatic improvement of precision of the distance to the LMC (i.e., those adopted in either Freedman et al. 2001; Pietrzyński et al. 2013), are meaningful; the distance to the megamaser host NGC 4258, in contrast, changed by ~5% between Herrnstein et al. (1999) and Humphreys et al. (2013) (used by Riess et al. 2011, 2016, respectively) and thereby, H_0 measurements and uncertainties anchored by either are not immediately comparable without consideration of these changes. Additional measurements with different anchors are given in Table 1 for completeness. By demonstrating the impasse between these techniques in Figure 1, we motivate the need for a third method; a detailed comparison between the "best" results from each method is provided in Riess et al. (2016).

[13] At the conclusion of the "Thanks to Henrietta Leavitt Symposium" on 2008 November 8, the attendees decided to adopt this nomenclature in honor of her significant contribution to this field. See https://www.cfa.harvard.edu/events/2008/leavitt/ for details.

Table 1
Recent Measurements of H_0 from CMB Modeling and the Distance Ladder

Short Title[a]	Technique	Notes	H_0 km s^{-1} Mpc^{-1}	Uncertainty km s^{-1} Mpc^{-1}	Reference
KP[b]	Cepheid	LMC Anchor, SNe Ia	71	2 (ran), 6 (sys)	Freedman et al. (2001)
KP[b]	Cepheid	LMC Anchor, Tully–Fisher	71	3 (ran), 7 (sys)	Freedman et al. (2001)
KP	Cepheid	Preferred Value	72	8	Freedman et al. (2001)
WMAP1	CMB	*WMAP* One-Year	72	5	Spergel et al. (2003)
WMAP3	CMB	*WMAP* Three-Year Mean	73.2	+2.1, −3.2	Spergel et al. (2007)
WMAP5	CMB	*WMAP* Five-Year Mean	71.9	+2.6, 2.7	Dunkley et al. (2009)
SH_0E^{2}S	Cepheid	LMC, Anchor	74.2	3.6	Riess et al. (2009)
SH_0ES[b]	Cepheid	LMC+MWπ Anchor	74.4	2.5	Riess et al. (2011)
SH_0ES[b]	Cepheid	NGC 4258, Anchor	74.8	3.1	Riess et al. (2011)
SH_0ES	Cepheid	Preferred Value	73.8	2.4	Riess et al. (2011)
WMAP7	CMB	*WMAP* Seven-Year Mean	70.4	2.5	Komatsu et al. (2011)
WMAP7[b]	CMB	*WMAP* +BAO+H_0 Mean	70.2	1.4	Komatsu et al. (2011)
CHP	Cepheid	LMC Anchor, MIR	74.3	1.5 (ran), 2.1 (sys)	Freedman et al. (2012b)
WMAP9	CMB	*WMAP* Nine-Year	70.0	2.2	Bennett et al. (2013)
WMAP9[b]	CMB	*WMAP* +eCMB+BAO+H_0	69.32	0.8	Bennett et al. (2013)
P2013	CMB	Planck+WP+highL	67.3	1.2	Planck Collaboration et al. (2014)
P2015	CMB	Planck TT+lowP+lensing	67.8	0.9	Planck Collaboration et al. (2015)
SH_0ES[b]	Cepheid	LMC, Anchor	71.82	2.67	Riess et al. (2016)
SH_0ES[b]	Cepheid	NGC 4258, Anchor	72.02	2.51	Riess et al. (2016)
SH_0ES	Cepheid	Preferred Value	73.00	1.75	Riess et al. (2016)
CMB Mean[c]	CMB	Unweighted	70.3	0.8	
Cepheid Mean[c]	Cepheid	Unweighted	73.4	0.4	

Notes.
[a] Label in Figure 1.
[b] Omitted from Figure 1.
[c] Note the mean is computed only for those results displayed in Figure 1.

others); (b) the need for additional trigonometric parallaxes to lay a more robust geometric calibration of the zero-point of the Leavitt law (see a prospectus for variable stars in the final *Gaia* sample in Eyer 2000); (c) contending with crowding at intermediate and large distances, especially by redder stellar populations that increase in relative brightness moving from the optical to the near- and MIR; and finally, (d) potential unknown changes in the reddening law as a function of metallicity and/or environment. Some of these concerns were largely minimized by moving into the MIR (e.g., the *Carnegie Hubble Program*; Freedman & Madore 2011; Freedman et al. 2012b, see our Figure 1), but tension between the Cepheid distance ladder and other techniques has remained.

Only about 800 Cepheids are known in the Galaxy, most of which are located in the solar neighborhood. *Gaia* is expected to observe up to 9000 classical Cepheids across the Galaxy to a limiting apparent magnitude $G \sim 20$ mag (Eyer 2000; Turon et al. 2012) and measure their parallax to better than $\sigma_\pi/\pi = 10\%$, on average, and to better than 1% for those located within 1–2 kpc (Turon et al. 2012). Beyond the Galaxy, *Gaia* will measure the parallaxes for at least 1000 of the brightest LMC Cepheids with $\sigma_\pi/\pi \sim 50\%$–100%, providing a probe of the Leavitt law at lower mean metallicity. In addition to the parallaxes, *Gaia* obtains metallicity estimates from $R = 11{,}500$ spectroscopy with the Radial Velocity Spectrometer for all stars brighter than $V \sim 16$ mag and permits study of star-by-star metallicity effects. The bulk of the Cepheids observed by *Gaia* are also accessible for independent high-resolution abundance studies from the ground (e.g., Luck & Lambert 2011, among others). In combination, such data sets will allow direct study of the various dependencies of the Leavitt law and permit improvement in the calibration of the Cepheid distance ladder in the future.

There are also challenges in estimating H_0 from measurements of anisotropies in the CMB. The microwave background data from which these measurements are derived are highly complex and require highly precise Galactic foreground removal as well as multiwavelength dust modeling: there is still debate regarding the effects on the resulting parameter fits (for instance, see discussion in Spergel et al. 2015). The power spectrum of CMB fluctuations derived from such maps is then modeled using six primary parameters that, hereto, have provided an excellent fit to existing data sets. However, in addition to the priors imposed on the parameters in the specific fitting procedure employed, there exist strong degeneracies in the *derived* cosmological parameters, and these covariant degeneracies are strongly coupled to H_0 (see discussion of such effects in Planck Collaboration et al. 2014). Moreover, comprehensive reanalysis by independent teams and detailed comparisons with complementary data sets (often at different frequencies or spatial resolutions) can produce significantly differing results (for instance see Addison et al. 2015), suggesting that there is still more to learn about methodology (both data and analysis) before the results can be interpreted at high confidence. Moreover, some authors have argued that, with the numerous complementary data sets available, the inclusion of additional parameters in the standard modeling is now feasible and perhaps, more appropriate (Di Valentino et al. 2015, 2016).

Table 2
Summary of Major Observational Programs Referenced in this Work

Program Name	Acronym	Primary Telescope	Proposal	Proposal ID	Distance Indicator
Carnegie Hubble Program	CHP	*Spitzer*	Freedman et al. (2008)	60010	MIR Cephieds Freedman et al. (2012b)
Carnegie RR Lyrae Program	CRRP	*Spitzer*	Freedman et al. (2012a)	90002	MIR RR Lyrae V. Scowcroft et al. (2016, in preparation)
Carnegie-Chicago Hubble Program	CCHP	*HST* *HST*	Freedman (2014) Freedman (2013)	13691 (GO) 13472 (SNAP)	NIR RR Lyrae + Optical TRGB NIR RR Lyrae

2. THE CARNEGIE-CHICAGO HUBBLE PROGRAM

To provide an independent route to H_0 and to increase the accuracy of the direct measurements of H_0, the Carnegie-Chicago Hubble Program (CCHP) aims to establish a new calibration of SNe Ia through the luminosity of the tip of the red giant branch (TRGB; Lee et al. 1993), as calibrated, in the first instance, by RR Lyrae stars. For clarity in placing this new program in the context of other efforts, Table 2 provides a summary of the major Carnegie-led efforts to measure the Hubble constant. The TRGB method is extremely precise and the underlying physics is well understood (e.g., Salaris et al. 2002, among others). Since galaxies of all morphological types host an ancient population of stars, the TRGB is a universally available Population II distance indicator. Moreover, RGB stars are found within all galactic structural components and are the dominant population in their low-density stellar halos. Stellar halos convey particular advantages for stellar population studies: (i) they are relatively immune to the vagaries of internal interstellar extinction, and (ii) since the stellar density drops with radius (see for instance Gilbert et al. 2012), concerns relating to crowding can be minimized.

The CCHP is designed to take advantage of the TRGB and build a fully independent, high-accuracy, and high-precision determination of H_0 based exclusively on Population II stars. This distance ladder is built using a combination of ground-based observations, archival *HST* observations, and new data acquired in a Cycle 22 GO proposal (Proposal 13691; Freedman 2014). The program is constructed such that the observations necessary for each rung are completed in a uniform fashion (i.e., using the same telescope and instrument combinations) to produce data sets designed specifically for the necessary measurements. Moreover, the CCHP can use archival data sets for its sample of tracer objects to test for and calibrate out any systematic effects. It is the objective of this paper to give a full overview of the steps required to build this independent distance ladder to provide context for the individual works to come.

Our distance ladder, built from Population II distance indicators, is currently constructed as follows:

1. We first use *HST*+ Fine Guidance Sensor (*HST*+*FGS*) trigonometric parallax distances to five Milky Way RR Lyrae variables (RRL) to set the zero-point of the *HST* NIR ($F160W$) RR Lyrae PL relation on a geometric basis. We have obtained new $F160W$ observations for these five stars that will be complemented with data from *Spitzer*, data from a ground campaign, and forthcoming measurements from *Gaia*. In addition, we are in the process of obtaining improved metallicities of Galactic star clusters to investigate the role of metallicity in the RR Lyrae PL (Section 3).
2. We then calibrate the TRGB absolute magnitude by applying the *HST* NIR PL relation to known RRL in the halos of six Local Group galaxies with a seventh calibration object from the megamaser distance to NGC 4258 (Section 4).
3. Next, we calibrate the absolute luminosity for SNe Ia by applying the TRGB calibration to determine the distance to their host galaxies (Section 5).
4. In the final step, we apply the SNe Ia calibration to the large population of SNe Ia that extend well into the pure Hubble flow by which we measure H_0 (Section 6).

Using reasonable estimates of the errors associated with each step and our sample size, this Population II distance ladder can reach an initial precision of 2.9%. We discuss individually our random and systematic uncertainties, and how they can be improved in the future in Section 7, in particular with the large set of trigonometric parallaxes obtained with *Gaia*. A summary is given in Section 8.

3. THE ABSOLUTE SCALE FOR GALACTIC RR LYRAE VARIABLES

The first rung of the Population II distance ladder is constructed using RR Lyrae variables in the Galaxy. RRL are evolved core-helium burning stars that have two primary subtypes, the RRab types that pulsate in the fundamental mode (i.e., with pulsational nodes at the core and edge of the star), and the RRc types that pulsate in the first overtone mode (i.e., with an additional pulsational node inside the star). They are typically old, with subsolar masses and periods that range from a few hours to one day (with RRc periods being shorter than RRab periods). Since the horizontal branch is, effectively, flat for some optical wavelengths (at which they were originally observed), the optical PL relationship is less immediately powerful than that for Cepheid-type variables. Distance determinations using the RRL are generally performed using the absolute mean visual magnitude (M_V) of the horizontal branch (as determined by the RRL) and the mean metallicity ([Fe/H]) of the population (the M_V–Fe/H relation, see Cacciari & Clementini 2003, pp. 105–122) rather than the direct utilization of the PL itself (for a review of the use of RRL for distance determinations see Bono 2003, pp. 85–104).

In their study of Galactic globular clusters at 2.2 μm, Longmore et al. (1986) first noted a correlation between period and the corresponding single-phase 2.2 μm magnitude for the RRL and suggested that there might exist a near-infrared (NIR) PL. Later, Longmore et al. (1990) used this first NIR PL to

Table 3
Properties of RR Lyrae Variables in the CCHP Galactic Calibration Sample

Target	Type	$\log(P_F)$	[Fe/H][a]	$\langle V\rangle$[a]	$\langle \boldsymbol{H}\rangle$[b]	A_V[c]	A_H[d]	π[a]	μ
SU Dra	RRab	−0.180	−1.80 ± 0.20	9.78	8.69 ± 0.03	0.03	0.01	1.42 ± 0.16	9.28 ± 0.24
RR Lyr	RRab	−0.247	−1.41 ± 0.13	7.76	6.61 ± 0.01	0.13	0.02	3.77 ± 0.13	7.11 ± 0.07
UV Oct	RRab	−0.266	−1.74 ± 0.11	9.50	8.30 ± 0.02	0.28	0.05	1.71 ± 0.10	8.84 ± 0.13
XZ Cyg	RRab	−0.331	−1.44 ± 0.20	9.68	8.79 ± 0.04	0.30	0.05	1.67 ± 0.17	8.89 ± 0.22
RZ Cep	RRc	−0.384[e]	−1.77 ± 0.20	9.47	8.06 ± 0.05	0.75	0.13	2.54 ± 0.19	7.98 ± 0.16

Notes.
[a] From Benedict et al. (2011).
[b] Derived from single *2MASS* phase points following the technique described in Section 3.1.3.
[c] From Feast et al. (2008).
[d] Assuming $A_H/A_V = 0.178$.
[e] $\log(P_F) = \log(P_{FO}) + 0.127$.

measure the distance to eight Galactic globular clusters in the K band. Extensive theoretical modeling demonstrated how the wavelength-dependent bolometric correction ultimately drives the behavior of the PL from the optical and into the infrared (Bono et al. 2001; Bono 2003, pp. 85–104; Catelan et al. 2004; Marconi et al. 2015). Moreover, the very tight mass–luminosity relationship for the horizontal branch phase of stellar evolution forces the PL to have a very small intrinsic width at these wavelengths (see Catelan et al. 2004). Thus, the use of the NIR PL in application to distances is particularly advantageous.

Several other significant advantages exist for observations of variable stars undertaken in the NIR:

1. the reduction of the effects of line-of-sight extinction by almost an order of magnitude ($A_H/A_V = 0.178$, see Cardelli et al. 1989);
2. the lower systematic impact of the possible non-universality of the reddening law;
3. the total amplitude of the light variation of the target star, seen in the NIR during its pulsation cycle, is greatly reduced due to the diminished contribution of temperature variation to NIR surface brightness (e.g., Longmore et al. 1990; Jones et al. 1996, among others);
4. the sinusoidal shape of the light curve due to the dominance by the radial variation effects in the NIR (see for instance Jones et al. 1988; Skillen et al. 1993; Smith 1995, among others);
5. the corresponding reduction in the intrinsic scatter of the PL relations (Madore & Freedman 2012), again because of the reduced sensitivity of infrared luminosities to temperature variations; and finally,
6. at the temperatures and surface gravities encountered for RR Lyrae variables, there are only a few metallic lines or molecular transitions in the NIR, so that atmospheric metallicity effects are predicted to be low. The CO bandhead within the IRAC 4.5 μm filter known to affect Cepheid light curves (e.g., Monson et al. 2012; Scowcroft et al. 2016) is not anticipated to have a significant effect for these temperatures. Furthermore, any remaining effects can be tested for and calibrated out.

Several recent and large-scale programs have begun to exploit the NIR and MIR (MIR) PL, including the Carnegie RR Lyrae Program (CRRP; Freedman et al. 2012a), the *Spitzer* Merger History and Assembly of the Stellar Halo (SMHASH; Johnston et al. 2013), the *VISTA* Variables in the Via Lactea project (VVV; Minniti et al. 2010), and the *VISTA* NIR YJK$_s$ Survey of the Magellanic Cloud System (VMC; Cioni et al. 2011). In this program, we will use the NIR PL as the foundation for a Population II distance ladder. Our first step is the precise calibration of the NIR PL for the IR channel of *HST*+*WFC*3; in particular, we use the *F*160*W* filter, which is similar to the more familiar ground-based *H*.

There are two primary concerns that are addressed at this stage: (i) the absolute *F*160*W* luminosity, i.e., the zero-point of the PL relation (Section 3.1), and (ii) and evaluation of scatter due to astrophysical effects *within* a population of RR Lyrae (Section 3.2). We use a set of Galactic RR Lyrae with preexisting parallaxes for the former, whereas for the latter, we explore a subset of RR Lyrae variables in the ω Centauri globular cluster. *Gaia* will deliver parallaxes with about 10 μas uncertainty for the 100–150 brightest RR Lyrae (those with $V < \sim$12.5 mag; de Bruijne et al. 2014; Clementini 2016) and will transform our understanding of both the absolute zero-point and the most effective method to account for astrophysical effects. For the purpose of this paper, we focus the discussion on the currently attainable precision for NIR observations of RR Lyrae and discuss sources of astrophysical uncertainty as they relate to our projected error budget, which is given in Section 3.3.

3.1. The Current Geometric Foundation of the RR Lyrae Distance Ladder

Trigonometric parallaxes have been obtained for five Galactic RRL using the *HST* Fine Guidance Sensor (*HST*+*FGS*; Benedict et al. 2011). The *Hipparcos* measurements for RR Lyrae were at its measurement limit; with the exception of RR Lyr ($\sigma_\pi/\pi \sim 18\%$), the over 100 RR Lyrae in *Hipparcos* have parallax uncertainties greater than 30% (with over 100 stars in the sample; see Clementini 2016). Practical constraints limited the application of *HST*+*FGS* to only the most nearby RR Lyrae. As such, trigonometric parallaxes were obtained for only five stars, of which four were type RRab (SU Dra, RR Lyr, UV Oct, and XZ Cyg) and one type RRc (RZ Cep). The properties of these five stars are given in Table 3.

3.1.1. Uncertainty in the PL zero-point

In Figure 2, we combine the Benedict et al. (2011) trigonometric parallaxes with NIR photometry from 2MASS (Skrutskie et al. 2006) and MIR photometry from the CRRP to demonstrate the NIR (J, H, K_s) and MIR (*Spitzer* 3.6 and

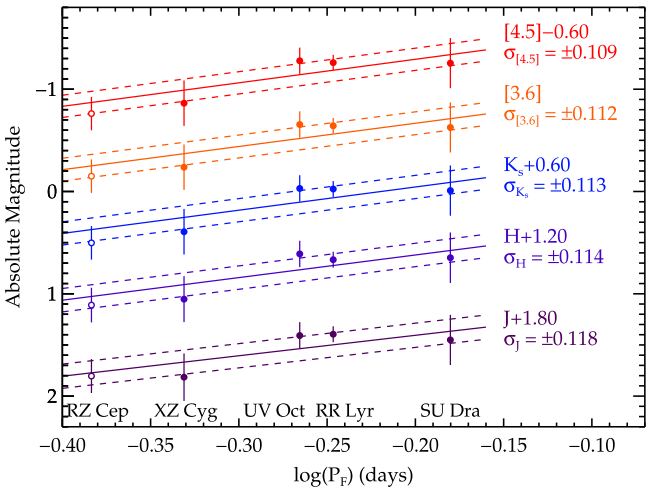

Figure 2. PL relations in the NIR and MIR for the five RR Lyrae variables with trigonometric parallaxes with *HST*+*FGS* from Benedict et al. (2011). There are four RRab type variables (filled circles) and one type RRc (open circle), which is plotted using its fundamentalized period (P_F, where $\log(P_F) = \log(P_{FO}) + 0.127$). The MIR data come from the CRRP and the NIR data are from 2MASS. Note the measurable slopes across the wavelength range and low intrinsic scatter ($\sigma_\lambda \sim 0.1$ mag), which is indicated with the dashed lines about each fit.

4.5 μm) PLs. The five stars give sparse sampling in $\log(P_F)$[14], and it is not feasible to determine the slope directly from the parallax sample. Thus, we adopt the PL slopes measured in M4 by (Braga et al. 2015, their Table 2) for the J (-1.739 ± 0.109), H (-2.408 ± 0.082), and K_s (-2.326 ± 0.074) and by (Neeley et al. 2015, their Table 3) for 3.6 μm (-2.332 ± 0.106) and 4.5 μm (-2.336 ± 0.105).

The adopted PL is overplotted in Figure 2 for each passband. We estimate the impact on our measurements from the uncertainty on the slope by performing a Monte Carlo simulation by varying the slope within its uncertainties and find a modulation of the resulting zero-point on the order of 0.002 mag or smaller for all bands. Because we define the zero-point of the PL relation at the midpoint of our $\log(P)$ distribution (here, $\log(P_F) = -0.30$), the effect of the slope uncertainty on the zero-point is effectively eliminated. Moreover, we test the full range of metallicity slopes in (see Muraveva et al. 2015 (see their Table 3 for a summary) and find no significant impact on the zero-point (defined at the midpoint of $[\mathrm{Fe/H}] = -1.58$ dex) for metallicity terms between 0.235 and 0.03 mag dex^{-1}. We suspect that the lack of an effect of the metallicity is due to the lack of a large metallicity span in the *HST* calibrators and that they are relatively clustered (see our Table 3). Thus, we neglect the metallicity term for this demonstration because the range of values for the effect in the literature is great, empirical studies are mainly limited to the K_s band at this time, and because we see no strong impact for our current RRL calibration sample (the individual uncertainties are much larger than the differential metallicity effect).

As shown in Figure 2, the variance about the PL for all passbands is approximately $\sigma_\lambda \sim 0.11$, although the mean uncertainty on the distance moduli is $\langle\sigma_\mu\rangle = 0.15$ mag (seven times larger than the mean apparent magnitude uncertainty of $\langle\sigma_H\rangle = 0.03$ mag; Table 3). As anticipated by the dominance of the parallax uncertainty to the total uncertainty in the absolute magnitude, the residuals for each band are highly correlated. Indeed, for RRc variables, the only independent measurement of the absolute magnitude by Kollmeier et al. (2013) is in 2.5σ tension with the Benedict et al. (2011) value for RZ Cep. This highlights the critical need for accurate and precise absolute magnitude measurements for RRL.

We compute the χ^2 statistic compared to the PL for each of our passbands, finding $\chi^2 = 0.39$, 0.40, 0.42, 0.38, and 0.36 for the J, H, K_s, [3.6], and [4.5], respectively. For the purposes of the following discussion we use $\chi^2_H = 0.40$ or the reduced chi-squared metric of $\chi^2_H \nu^{-1} = 0.1$ (where ν is the number of degrees of freedom), which is representative of results for all bands. For $\chi^2\,\nu^{-1} < 1$, the implications are that (i) the model is incorrect, (ii) the uncertainties follow a non-Gaussian distribution, (iii) the uncertainties are improperly assigned (i.e., Bevington & Robinson 2003, chapter 11), or (iv) the intrinsic variance of a sample has not been accounted for (i.e., Bedregal et al. 2006, their Section 3.1). We can evaluate each of these possibilities.

For the first option, our adopted PL is supported by several studies of the PL for globular clusters (Braga et al. 2015; Neeley et al. 2015 being the most recent), and thus our model is representative of the behavior of NIR and MIR RR Lyrae. We did neglect metallicity, but accounting for this would only *reduce* the measured variance and, using the maximal estimate for the metallicity component (Bono et al. 2001), in the K band, we obtain an effect of 0.07 mag, which, when removed, only lowers the measured variance to 0.08 mag. For the second option regarding the nature of the uncertainties, discussions involving the uncertainty for the reference frame in (Benedict et al. 2011, their Figure 4) imply that the final uncertainties are, indeed, Gaussian in nature using their procedure. For the third possibility, we use the analysis of Benedict et al. (2002, their Figure 7), in which the results for the early *HST*+*FGS* parallax program were compared to *Hipparcos*, from which the authors conclude that it is likely that the uncertainties for the *HST*+*FGS* parallaxes are overestimated by a factor of ∼1.5. Comparing Benedict et al. (2002) to Benedict et al. (2011), we find no significant change of procedure that would have altered the conclusion reached by this comparison.

For the fourth possibility, we undertake a series of Monte Carlo simulations, described in detail in a forthcoming publication focused on the zero-points, to understand the interplay between the intrinsic dispersion about the PL and the parallax uncertainties in a statistical sense. These simulations use a well-measured PL as a fiducial by which to compare the parallax uncertainties. Even with the intrinsic variance of the PL included, the resulting variance of the fits is still statistically inconsistent with the input uncertainties (i.e., $\chi^2_H \nu^{-1} < 1$). If the parallax errors are scaled by 50%, our simulations produce final variances consistent with those measured in Figure 2 with $\chi^2_H \nu^{-1} \sim 1$. Thus, comparison of the *HST*+*FGS* parallaxes to two independent fiducial measurements, *Hipparcos* and the well-established NIR PL, indicate that the uncertainties are overestimated by ∼50%.

Our assessment is consistent with prior works that employed the *HST*+*FGS* parallax program for distance scale applications using both Cepheids and RR Lyrae (for instance, Freedman et al. 2012b; Braga et al. 2015; Muraveva et al. 2015; Neeley et al. 2015; Clementini 2016, among others). For the purpose of forecasting an error budget for the CCHP, we scale the

[14] Where P_F is the fundamental period, for which the first-overtone pulsators are fundamentalized by the expression $\log(P_F) = \log(P_{FO}) + 0.127$.

dispersion, $\sigma = 0.11$ mag, about the PL shown in Figure 2 by 50%, to project that $\sigma = 0.05$ mag is statistically consistent with current data. While these statistical arguments are compelling, they are not conclusive. Owing to the release of initial parallaxes for objects common to *Hipparcos* in the near future (see Michalik et al. 2015), a more exhaustive exploration of the zero-point for the NIR+MIR PL (and perhaps a better understanding of the Benedict et al. uncertainties) will be feasible at a later stage of our program.

3.1.2. HST Observations of Galactic RR Lyrae

We have obtained randomly phased observations of the five galactic RR-Lyrae with known geometric parallaxes with *HST*+*WFC3/IR* in the *F160W* filter in our Cycle 22 GO proposal (five stars; proposal 13691; Freedman 2014). Given the relatively bright apparent H magnitudes of these stars, ranging from $\langle H \rangle = 6.67$ to $\langle H \rangle = 8.79$ (Table 3), special observing techniques were required that are sufficiently technical to be beyond the scope of this work. A full presentation of this stage of our program will be given in J. Rich et al. (2016, in preparation).

Obtaining even a single-phase point requires a full *HST* orbit, and attaining full phase-coverage of these stars is prohibitively expensive (i.e., ~12 individual points corresponds to ~12 orbits per star). Thus, we are limited to single-phase points for these stars. In the next section, we discuss a method for determining accurate mean magnitudes from single-phase observations, using existing high-cadence light curves for at least two optical wavelengths.

3.1.3. RR Lyrae Light Curve Fitting for Predictive Templates

To estimate the mean magnitudes of our Galactic RRL calibrators directly from the *F160W* observations, we employ a technique that uses well-sampled optical light curves to generate a template suitable for longer wavelength data. Instead of using Fourier fits modeled to high-cadence NIR observations for select stars (i.e., as in Jones et al. 1996), we will use high-cadence observations in multiple optical bands to derive NIR and MIR light curve templates for each individual star *from its own optical light curve*. This technique has the advantage of capturing the specific color-structure of an individual RR Lyrae's light curve.

Our template technique was first developed for Cepheids by Freedman (1988) and Freedman & Madore (2010a), and requires high-cadence optical (B, V, I) time-series data. We have initiated an observational survey to obtain such data and derive templates for individual stars that will be fully described in a series of forthcoming publications (the optical data, not including the new *HST* observations, in A. Monson et al. 2016, in preparation and the template technique in R. Beaton et al. 2016, in preparation). To demonstrate the technique and its role in the CCHP, we present data from our optical campaign for RR Gem of RRab type in Figure 3.

The optical light curves for RR Gem are given in Figure 3(a) for the B, V, and I broadband filters. These optical luminosity variations are sensitive to two physical effects that change due to the pulsations: (i) temperature and (ii) radius. The temperature variability can thus be isolated using the optical color as a proxy for temperature. The optical color curves for RR Gem are given in Figure 3(b) for $(B-V)_0$, $(V-I)_0$, and $(B-I)_0$.

With the temperature effect constrained by color curves, it is then possible to remove it from the optical light curves and thereby isolate the component that is due to radial variations. The residual curves after a scaled subtraction of the color curves, called the F magnitude by Freedman & Madore (2010a), are given in Figure 3(c) for each of the color curves in Figure 3(b). These F curves predict the shapes of the NIR and MIR light curves, modulo scale factors (see discussion in Freedman & Madore 2010a). Figure 3(d) compares the NIR and MIR light curves predicted from the F magnitude to K_s and J photometry from Liu & Janes (1989) and MIR photometry from the CRRP, which show very good overall agreement.

We can compute the shift between our template light curve in a given photometric band and the single-phase point to adjust the photometric zero-point of our template, as is demonstrated for the 2MASS photometry of RR Gem in Figure 3(d). With the zero-point shift, the template can then be used to determine the appropriate mean intensity in a given band. Thus, from a single-phase point for the CCHP in the *F160W* filter, we can determine reliable mean magnitudes. Example preliminary measurements from our *HST* SNAP proposal (PID 13472; Freedman 2013) in *F160W* are also plotted in Figure 3(d) for RR Gem and show overall agreement with the ground-based H curve (we note that RR Gem had only few of the complications of the significantly brighter *HST* RRL calibrators and was chosen as a demonstration object for this reason).

The application of this method requires knowledge of the ephemeris of an RRL (time of maximum light, period, and any period-change related terms) to high precision. Our optical campaign is sufficiently well sampled that when tied into literature observations, we are able to test and revise the ephemerides for our RRL calibrator stars and be relatively confident in our phasing (A. Monson et al. 2016, in preparation). The uncertainty in the mean magnitude is a function of phase (ϕ) and will be discussed in R. Beaton et al. (2016, in preparation). The mean H magnitudes and uncertainties for the RRL calibrators in Table 3 and used in Figure 2 were determined from a single 2MASS observation from this technique.

3.2. Assessing the Scatter About the PL

Our key concern at this state of the CCHP is the precision to which we can measure the distance to our Local Group targets (see Table 4, bottom section). Our Local Group targets span a range of [Fe/H] from −1.68 dex (Sculptor) to −0.44 dex (M32), with a mean and median metallicity of −1.3 dex and −1.5 dex, respectively (values based on the M_V–[Fe/H] relationship for the RRL in our pointings are given in Table 4, unless otherwise noted). Thus, our Local Group sample is relatively well matched to the mean metallicity of our five RRL calibrators ($\text{median}_{[\text{Fe/H}]} = -1.58$ dex). Our distance precision is limited by sources of scatter that are either observational (i.e., measurement) or astrophysical in nature. For the former, typical effects are photometric accuracy, repeatability, and crowding, which generally can be identified and controlled for an individual data set. For the latter, there are numerous physical factors that add scatter to the PL, including but not limited to (i) chemical abundances, (ii) the evolutionary state, and (iii) changes in period (e.g., Smith 1995; Cacciari 2013).

Diagnosis of such astrophysical complications requires independent data sets or specialized statistical methods to be

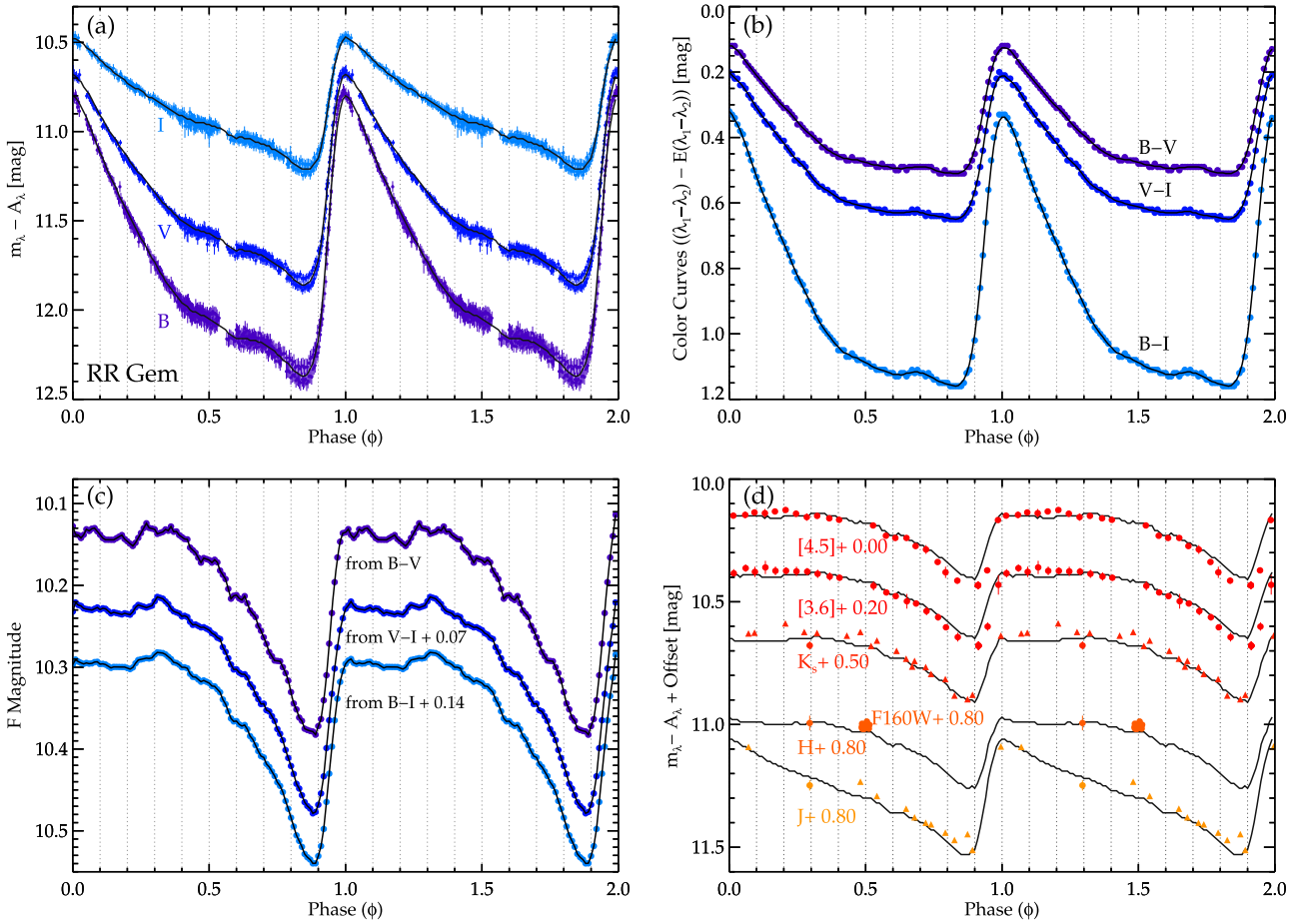

Figure 3. Construction of light-curve templates. (a) Observed optical light curves for RR Gem in *B*, *V*, *I*. (b) Color curves for RR Gem that physically trace the temperature variations over the pulsation cycle. (c) By removing the temperature curves from the initial light curves, the radial variations can be isolated. These radial variations are the only dominant effect seen in the NIR and MIR. (d) NIR and MIR light curve templates generated from the optical data (black lines) with sparsely sampled MIR data overplotted (colored points). For *J* and K_s we show both the *2MASS* data (filled circles) and data from Liu & Janes (1989) (filled triangles). For *F*160*W* (similar to *H*), we show all of the individual measurements obtained using our *HST* observing strategy for this bright star (described in Section 3.1.2). Note the reduced light-curve amplitudes and overall more sinusoidal shape at these wavelengths. Using the templates, we can produce high-quality intensity-weighted mean magnitudes even with only sparsely sampled or single-phase observations.

properly taken into account (see discussion in Sandage et al. 2015, their Appendix B). Unfortunately, for our Local Group targets such independent measurements are prohibitively expensive for all of the six objects; the mean magnitude of an RR Lyrae at M31 distance is $V \sim 25.5$ mag, which is out of reach for current high-resolution spectroscopy and requires *HST* or imaging on an >8 m facility for high-quality temporal monitoring. Thus, to understand the role of these astrophysical effects on the precision of our Population II distance scale, we can only account for them in a statistical fashion. With comparison of the scatter about a local well-characterized "ideal" PL to a local well-characterized analog to our Local Group RR Lyrae targets, it is possible to make such a measurement.

To assess the scatter about the PL for our NIR data, we compare the *H* PL for the LMC star cluster Reticulum to that of the star cluster ω Centauri. Reticulum is a cluster (i) of low central concentration (Walker 1992), (ii) of mono-abundance ($[Fe/H] = -1.57 \pm 0.03$; Grocholski et al. 2006), (iii) with an apparent single stellar population (Mackey & Gilmore 2004), (iv) that is located $\sim 11^\circ$ from the LMC center (Walker 1992), and (v) has low apparent foreground and background contamination (Mackey & Gilmore 2004). In contrast, ω Centauri is one of the most massive and metal-rich star clusters with a wide metallicity spread for its RR Lyrae ($-2.5 < [Fe/H] < -1.1$; Rey et al. 2000; Sollima et al. 2008) and a rather complex horizontal branch morphology (for discussion see Gratton et al. 1986). Moreover, while we have "recent" NIR light curves that can be used to correct for shifts in period for individual stars in Reticulum (a detailed description of how this is done in application to our Galactic RRL calibrators will be given in A. Monson et al. 2016, in preparation), we did not make such changes in ω Centauri. The median [Fe/H] for Reticulum and ω Centauri are well matched to the median of our Local Group sample. Moreover, the total range of metallicity in ω Centauri is also comparable to the total range of our Local Group sample, although it is more metal-poor overall (see Table 4). Thus, a comparison of the PL scatter between these two systems provides a meaningful estimate of the added uncertainty that is due to astrophysical scatter in the RRL populations we anticipate for our Local Group sample.

Figure 4(a) compares the *H* PL for Reticulum and ω Centauri using image data collected with the FourStar camera on the Baade 6.5 m telescope at Las Campanas Observatory (Persson et al. 2013) and mean magnitudes determined from GLOESS fitting (see discussion in Persson et al. 2004). The data for both clusters are overall of the same quality (i.e., despite the larger distance to Reticulum, the same signal-to-noise ratio is

Table 4
Summary of New Observations Obtained for the RRL Stage of the CCHP

Target	Class	⟨[Fe/H]⟩[a]	Supplementary Imaging	$F160W$ (N_{obs})	N_{RRL}	RR Lyrae Discovery
RR Lyrae zero-point—						
RR Lyr	Galactic RRab	-1.41 ± 0.13	TMMT	2 Random	⋯	⋯
RZ Cep	Galactic RRc	-1.77 ± 0.20	TMMT	2 Random	⋯	⋯
UV Oct	Galactic RRab	-1.47 ± 0.11	TMMT	2 Random	⋯	⋯
XZ Cyg	Galactic RRab	-1.44 ± 0.20	TMMT	2 Random	⋯	⋯
SU Dra	Galactic RRab	-1.80 ± 0.20	TMMT	2 Random	⋯	⋯
Metallicity Effects—						
ω Centauri	Cluster	−2.5 to −1.1	*Magellan*+FourStar	2 Random	34	Sollima et al. (2008)[b]
TRGB zero-point—						
Sculptor	dSph	−1.68[c]	*Magellan*+FourStar	2 Random	52	Kaluzny et al. (1995)[d]
Fornax	dSph	−0.99[c]	*Magellan*+FourStar	2 Random	105	Bersier & Wood (2002) Mackey & Gilmore (2003)
IC 1613	IB(s)m	−1.60[c]	⋯	12 Phased	67	Bernard et al. (2010)
M32	compact E2	−0.44	⋯	12 Phased	305	Fiorentino et al. (2012)
M31	SAB(s)b	−1.50	⋯	12 Phased	256	Sarajedini et al. (2009)
M33	SA(s)cd	−1.48	⋯	12 Phased	69	Sarajedini et al. (2006)

Notes.
[a] Galactic RRL metallicities are from Benedict et al. (2011) and Local Group metallicities from Column 7, unless otherwise noted.
[b] The most recent compilation of ω Centauri RR Lyrae is Navarrete et al. (2015).
[c] Mean stellar metallicity for RGB stars with medium-resolution spectroscopy from the compilation of McConnachie (2012) for Sculptor and Fornax and from detailed main sequence fitting for IC 1613.
[d] The most recent compilation of Sculptor RR Lyrae is Martínez-Vázquez et al. (2015).

reached). As in Section 3.1.1, we adopt an H period slope from Braga et al. (2015) for the fundamental period (P_F). The study of Sollima et al. (2006) for 16 star clusters found no significant difference in the slopes for clusters spanning a range of nearly 2 dex in [Fe/H]—a very similar span as for ω Centauri (see Table 4). Since the goal of this demonstration is to study the scatter and not the zero-point itself, we neglect a correction for the mean metallicity for either system because it only modulates the absolute magnitude of the zero-point (Marconi et al. 2015; Muraveva et al. 2015). We limit the ω Centauri sample to those stars outside of the ω Centauri half-light radius (Trager et al. 1995, i.e., $r < 5'$)[15] to avoid complications from crowding in its very dense inner regions. We are left with a sample of 81 stars in ω Centauri and 26 stars in Reticulum.

We determine residuals about the PL as the difference between the magnitude of a given source and its magnitude were it on the PL relation (i.e., vertical from the PL in Figure 4(a)). A normalized marginal distribution for the residuals is shown in Figure 4(b) for Reticulum and in Figure 4(c) for ω Centauri. From a comparison of Figures 4(b) and (c) it is clear that the residuals for ω Centauri show a much larger overall variance than those of Reticulum. For Reticulum, we measure a scatter of $\sigma_{tot} = 0.04$ mag with a median H magnitude uncertainty of $\sigma_{meas} = 0.02$ mag, and for ω Centauri, we measure $\sigma_{tot} = 0.07$ mag with a median H magnitude error of $\sigma_{meas} = 0.02$ mag. We now use these variances to isolate the component in ω Centauri from astrophysical effects. We note that this approach to estimating the effect requires no assumption of the underlying distribution for the residuals from any one source.

Based on the evidence summarized previously, it is not unreasonable to assume that Reticulum represents a system for which the astrophysical sources of scatter (metallicity, evolution, and period shift) are minimal. For Reticulum, the total variance, σ^2_{tot}, is the quadrature sum of the variance that is due to measurement uncertainties (σ_{meas}) and the intrinsic width of the PL (σ_{int}). Thus, we can derive an upper limit on the intrinsic variance as

$$\sigma_{int} < \sqrt{\sigma^2_{tot} - \sigma^2_{meas}}, \quad (1)$$

from which we estimate that the intrinsic width of the PL is $\sigma_{int} < 0.03$ mag.

The total variance ω Centauri must include an additional term for astrophysical effects (σ_{astro}). We can similarly determine an upper limit on the added variance that is due to the combination of these astrophysical effects as

$$\sigma_{astro} < \sqrt{\sigma^2_{tot} - \sigma^2_{meas} - \sigma^2_{int}}, \quad (2)$$

from which we estimate that the additional scatter in ω Centauri from astrophysical effects is $\sigma_{astro} < 0.06$ mag, using our estimate of σ_{int} from Reticulum.

In application to our Local Group RRL sample, we proceed to adopt an uncertainty due to astrophysical effects of $\sigma_{astro} < 0.06$ mag in the H band based on our comparisons to ω Centauri. We will probe this effect directly in the $F160W$ magnitudes by observing a subset of ω Centauri RRL and combining these single-phase observations with our FourStar H templates to derive mean magnitudes (see Table 4). A more in-depth look at these effects requires a larger sample of individual spectroscopic metallicities common to our NIR data set and one that fully samples the multiple stellar populations in ω Centauri.

3.3. Current Error Budget for the RR Lyrae

Assuming the intrinsic dispersion for a multiabundance population is best matched to that of the total scatter in ω Centauri, we adopt $\sigma_{astro} = 0.06$ mag from ω Centauri for the

[15] As presented in Harris (1996a, 1996b) and updated online versions of the compilation.

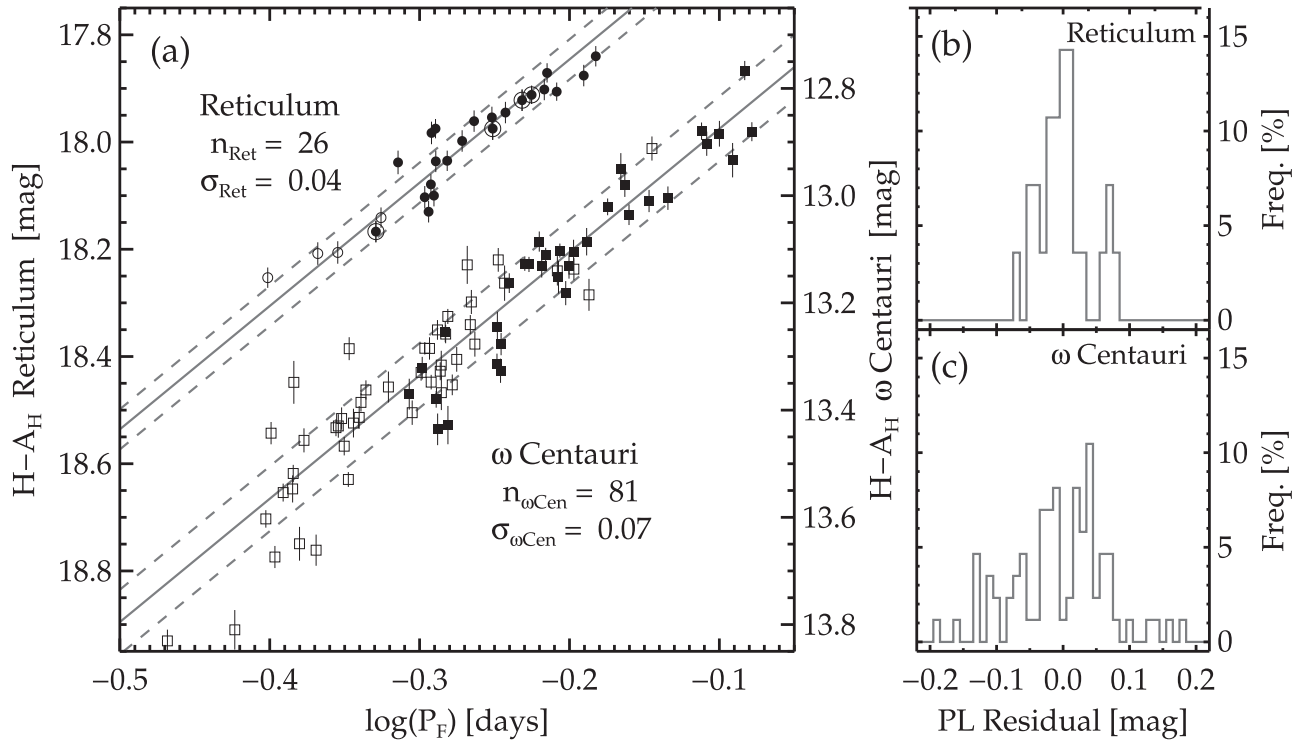

Figure 4. Scatter about the *H* PL. (a) Near-infrared (*H*) period–luminosity relations for 26 RR Lyrae variables in the Reticulum cluster with a scatter of only ±0.04 mag (upper) and for the 81 least crowded RR Lyrae variables in ω Centauri, showing a scatter of only ±0.07 mag (lower). In the plot, the open symbols denote RRc type variables, and filled symbols denote RRab type variables. There are four RRab pulsators with the Blashko effect in Reticulum, these are indicated by a larger open circle. Solid lines show the fitted PL relationships based on the slope determined from the Galactic globular cluster, M4 (Braga et al. 2015), and dashed lines show the ± 1σ ranges about the PL. This intercomparison places an upper limit on the contribution of effects that are astrophysical in nature (metallicity, evolutionary state, etc.) to the observed scatter in ω Centauri. (b) Marginal distribution of PL residuals for Reticulum with a scatter of $\sigma = 0.04$ mag. (c) Marginal distribution of PL residuals for ω Centauri with a scatter of $\sigma = 0.07$ mag.

intrinsic scatter term in our preliminary uncertainty estimate for the Local Group RRL pointings. This term will be evaluated on a case-by-case basis for each of our RRL pointings in the H_0 error budget at the conclusion of our program. This is then coupled with the uncertainty of our zero-point discussion for *H* ($\sigma_{\rm fit} = 0.05$ mag), and we project a total uncertainty on the determination of a given distance using the PL of $\sigma_{\rm total} = 0.079$ mag. Converting into the error on the mean ($\sigma_{\rm total}/\sqrt{(5)}$), we find an uncertainty on the mean of 0.036 mag, or 1.7% in distance. Adopting instead the scatter from a mono-abundance population from Reticulum of $\sigma_H = 0.04$ mag, we project an uncertainty on the mean of 0.030 or 1.4% in distance. At this stage in our program, in advance of the anticipated results from *Gaia*, we select the conservative 1.7% zero-point uncertainty for the RR Lyrae *F*160*W* PL zero-point for our preliminary error budget.

4. THE ABSOLUTE SCALE FOR THE TRGB

The next step in the CCHP distance ladder is to determine the absolute magnitude of the TRGB. The red giant branch terminates with a sharp discontinuity in its luminosity function that, when calibrated, can be used as a standard candle. This truncation of the RGB luminosity function is the result of the sudden lifting of degeneracy and rapid onset of helium burning throughout the isothermal core of the most luminous RGB stars that represents the end of the RGB evolutionary phase (Salaris & Cassisi 1997). *I*-band observations of the TRGB have empirically shown this feature to be very well delineated (e.g., Lee et al. 1993; Sakai et al. 2004; Caldwell 2006; Rizzi et al. 2007; Mager et al. 2008, among others). The TRGB can be determined by either applying edge-detection techniques to the luminosity function on the RGB (i.e., Lee et al. 1993) or fitting a modeled luminosity function to the observed luminosity function, when asymptotic giant branch (AGB) and RGB populations cannot be separated (i.e., Méndez et al. 2002). The detailed study of Rizzi et al. (2007) furthered the technique as a high-precision distance indicator, where the precision is ultimately related to the number of stars near the TRGB (as demonstrated explicitly in Madore & Freedman 1995; Madore et al. 2009).

A number of calibration issues remain to be addressed to take the TRGB method beyond its current precision to that of utility for our program (the 1σ dispersion of the *I*-band magnitude at the tip is estimated at $\sigma_{M_I} \pm 0.12$ mag; Bellazzini 2008); the CCHP was explicitly designed to undertake a systematic study of these issues. The TRGB has an expected, but modest, dependence on metallicity; however, an exact determination of the absolute magnitude of the TRGB has remained challenging within the Milky Way. Galactic globular clusters were the first objects used to determine the zero-point (beginning with Da Costa & Armandroff 1990), but at the level of accuracy we are now seeking, there are many issues to address: the distances to the globular cluster hosts themselves are uncertain due to main-sequence fitting uncertainties and line-of-sight reddening corrections, on top of the systematic uncertainties in adopting a (multiabundance-dependent) fiducial main sequence. Of greater concern is the fact that there is no guarantee for any given globular cluster that there will be enough giants currently ascending the RGB to fully populate

the brightest part of the luminosity function, thus leading to a systematic underestimate of the luminosity of the TRGB. For the CCHP, we will determine the absolute magnitude of the TRGB relative to other distance indicators in Local Group galaxies, in particular the RRL.

We now discuss our plans to set the absolute zero-point of the TRGB method using two independent paths: (a) Using the geometric distance to the circumnuclear maser disk in the active galaxy NGC 4258 (Section 4.1), and (b) applying the parallax-based Galactic RRL NIR PL relation to the halo populations of six Local Group galaxies (Section 4.2). The error budget from this stage of the Population II distance ladder is given in Section 4.3. In the future with *Gaia*, we can bypass the RRL distance scale entirely and calibrate the TRGB directly (Section 7.3).

4.1. Path 1—The Geometric Distances to the Megamaser Host NGC 4258

Currently, the only technique capable of measuring geometric distances outside of the Local Group is using H_2O megamasers that are found in the accretion disks around central black holes. If seen approximately edge-on and tracked over time, the individual maser sources can be used to trace the dynamics within the accretion disk, and, under the assumption of Keplerian motion, constrain the line-of-sight distance to the host galaxy using geometry.

NGC 4258 is the only galaxy near enough to be used as a TRGB calibrator. It has a geometric distance derived from the kinematics of its circumnuclear maser disk (Humphreys et al. 2013). Modeling of the accretion disk using the detailed kinematical data produces a line-of-sight distance of $d_{\rm NGC\,4258} = 7.60 \pm 0.17$ (random) $\pm$ 0.15 (systematic) Mpc or $\mu_{\rm NGC\,4258} = 29.40 \pm 0.05$ (random) $\pm$ 0.04 (systematic) mag.

Mager et al. (2008) measured TRGB stars in the halo of this same galaxy using *HST* + ACS observations (Madore 2002, PID 9477), specifically designed to target its Population II rich stellar halo. Figure 5(a) demonstrates the location of the *HST* + ACS field, and Figure 5(b) presents the exquisite red giant branch with a highly resolved TRGB. We note that the metallicity dependence of the TRGB, which is projected into a color dependence in the CMD, has been calibrated out of Figure 5(b) following the procedure discussed in Mager et al. (2008) and more formally presented in Madore et al. (2009). The results of applying an edge-detection algorithm to the luminosity function is shown Figure 5(c) and determines the TRGB at $I = 25.24 \pm 0.04$ (Mager et al. 2008).

Combining the maser distance with the TRGB estimate, we obtain an absolute magnitude for the $M_I^{\rm TRGB} = -4.16 \pm 0.06$ (random) $\pm$ 0.04 (systematic) mag. This value is broadly consistent with other calibrations of the TRGB, $M_I^{\rm TRGB} = -4.04 \pm 0.12$ mag for [Fe/H] $= -1.52$ (Bellazzini et al. 2001, 2004), which is the relation used by Mager et al. (2008) to calibrate the dependence of the TRGB on metallicity, but is slightly offset. We note that the initial maser distance at the time of the Mager et al. (2008) from Herrnstein et al. (1999) was entirely consistent with both the TRGB and Cepheid based distances.

Within the context of the CCHP, we use these existing observations to provide a direct calibration of the TRGB, beyond those shown in Table 5. More specifically, we are reanalyzing these archival data to ensure identical image processing techniques and photometry are employed. We plan to calibrate the TRGB in the native *F*814*W* *HST*-ACS flight magnitude system to eliminate uncertainties imposed by filter conversions.

4.2. Path 2—The Local Group RR Lyrae Variables

Using the RR Lyrae PL discussed in the previous section, we can determine precise distances to Local Group galaxies. Each of these Local Group galaxies has a stellar halo rich in resolved Population II RGB stars, and we can thereby place the TRGB absolute magnitude firmly onto the RRL geometric distance scale.

We have selected galaxies in the Local Group that have known and well-characterized RRL (i.e., with light curves sufficient to identify the pulsation mode and to determine the period). To avoid effects from multiple populations, line-of-sight depth, and differential extinction, among others, we explicitly opt to exclude the LMC or the inner regions of other nearby star-forming galaxies that are not seen face-on. Imposing these requirements yields six nearby galaxies: M31, M32, IC 1613, M33, Sculptor, and Fornax, which have the prerequisite discovery data with *HST*+ACS (published in the literature; specifics are given in Table 4). Owing to the galactic demographics of the Local Group, five of our six calibrators are dwarf galaxies, but given that these systems are the primary building blocks of the galactic halos we will probe in the SNe Ia hosts, the stellar content of these dwarf galaxies is likely representative of these larger galaxies.

4.2.1. New HST Observations

As discussed in Section 3.3, we have used the *HST*+WFC3–IR channel with the *F*160*W* filter for our studies of the RR Lyrae. As in the CHP-I for Cepheids (for example light curves see Scowcroft et al. 2011; Monson et al. 2012), we obtain 12 phase points that are used with our template fitting techniques (Section 3.1.3) to determine the phase-weighted mean magnitudes. This combination of these two techniques can produce mean magnitudes at the 2% level for individual stars (see detailed discussions in Madore & Freedman 2005; Scowcroft et al. 2011). Example data from our pointing in IC 1613 are given in Figure 6, where Figure 6(a) shows the pointing map (the *HST*+WFC3–IR pointing has a smaller FOV), and example light curves in *F*475*W* (blue), *F*814*W* (red), and *F*160*W* (black) for RRab and RRc variables in IC 1613 are shown in Figures 6(b) and (c), respectively. The data presented in Figures 6(b) and (c) will be presented in full by in D. Hatt et al. (2016, in preparation) and include a comparison to published works using other methods in addition to our first estimate of the *F*160*W* TRGB zero-point. Figure 6 demonstrates that we have sufficient light curve sampling to determine mean magnitudes to high precision.

The RRL observations for each of the six galaxies are effectively identical, with the exception of Fornax and Sculptor (to be discussed below), and are summarized in Table 4. Fields were chosen to have about 100 RR Lyrae that were previously characterized in at least two optical photometric bands. We anticipate that some fraction of the objects in each field will be blended or crowded due to both the change in resolution from their detection in *HST* + ACS at $0\farcs05$ pixel^{-1} to *HST* + WFC3–IR at $0\farcs135$ pixel^{-1} and to the increase in the relative brightness of the AGB populations at this wavelength.

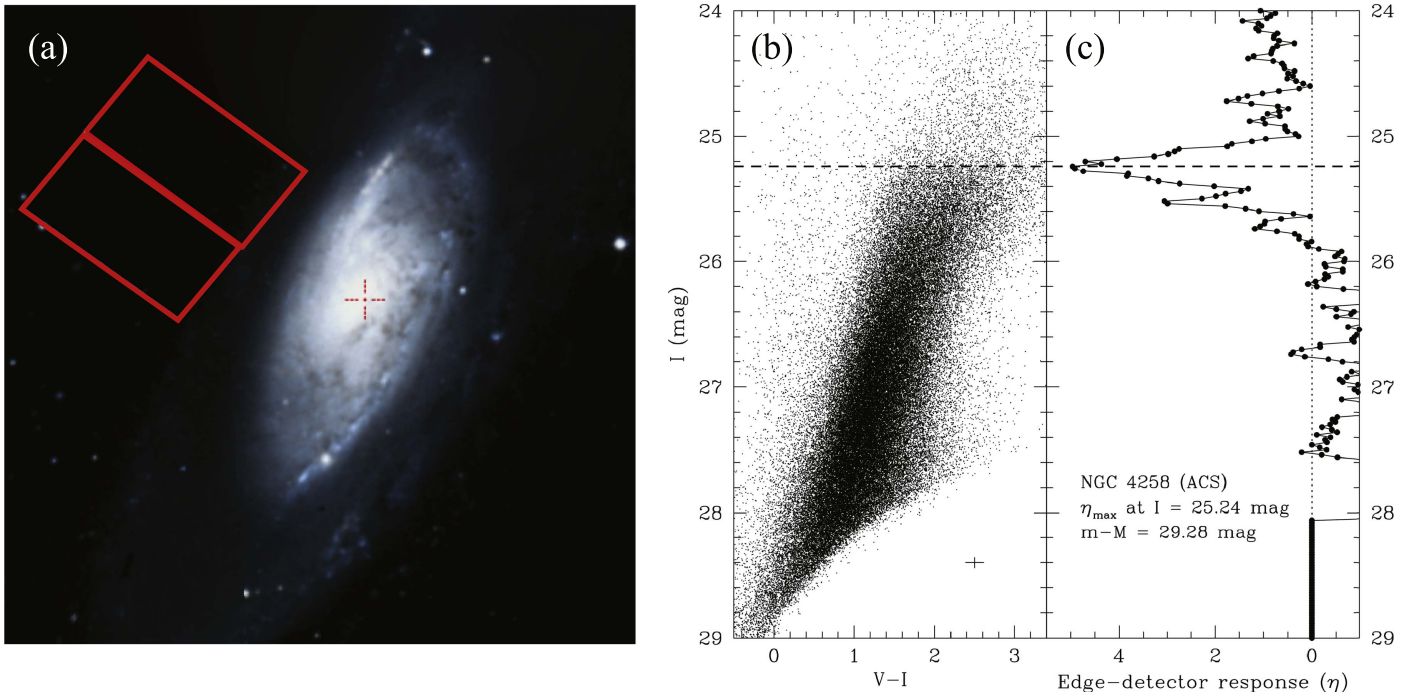

Figure 5. Example TRGB detection in NGC 4258. (a) The location of the *HST*+ACS pointing of Mager et al. (2008) (blue outline) relative to the disk of NGC 4258 (from DSS) used to determine the TRGB distance to NGC 4258, emphasizing its placement securely in the halo of NGC 4258. (b) The *HST* + *ACS V*,*I* CMD in the halo of NGC 4258 reveals a high-contrast TRGB detectable in a galaxy with $\mu > 29.0$ mag. (c) The corresponding response of an edge-detection filter, effectively the first derivative of the *I* luminosity function, applied to the CMD shows a large peak consistent with the visual impression of the TRGB (dotted line). The *I* magnitude has been adjusted for metallicity effects. Reproduced from Mager et al. (2008).

To cover the majority of the original *HST* + ACS field, two *HST* + WFC3–IR fields are required per single *HST* + ACS field, and we optimized the placement of these fields to maximize the total number of RR Lyrae. We also intentionally placed some overlap between the two fields to test for systematic effects.

The RRL observations for ω Centauri, Fornax, and Sculptor are designed to obtain closely spaced phase points during a single *HST* orbit in $F160W$. For both Fornax and Sculptor, parallel ACS observations for the purpose of the TRGB are also obtained, as is discussed in Section 4.2.2 (exposures in ω Centauri were too frequent to permit parallel observations due to data transmission rates). The RRL observations will be combined with literature optical light curves (see Figure 4), and the self-template technique of Section 3.1.3 is applied to determine mean magnitudes.

For the TRGB observations, the Local Group targets can be split into two categories: those of low surface brightness and those of high surface brightness. For the low surface brightness galaxies, a single ACS field does not have sufficient sampling of the TRGB, and the photometry for these objects has been supplemented with ground-based observations (Section 4.2.2). For the high surface brightness galaxies, the ACS field does have sufficient statistics to measure the TRGB directly, as we now describe. The TRGB data for the Local Group objects are obtained with ACS in parallel mode to the RRL data previously described.

We constrained the roll angle of the *HST* observations such that the ACS field occurs at larger object-centric radii, both safely within their halos and at sufficiently low stellar density to avoid significant crowding. For clarity, we include an example Local Group pointing in Figure 6(a) for IC 1613 to demonstrate the coupled observations and their relationship to the archival *HST* imaging. We are also using imaging data from the archived *HST* RRL discovery programs (as noted in Table 4) to measure directly the TRGB magnitude in these fields to improve statistics and check for slight differences, if any, in crowding and metallicity between the fields.

4.2.2. Supplementary Wide Field Observations

Sculptor, Fornax, and IC 1613 are each dwarf galaxies with intrinsically low stellar density. While wide-field observations that contain the full extent of the galaxy (to several half-light radii) sufficiently sample the TRGB, our relatively small ACS field ($4' \times 4'$) samples a relatively small area of these nearby systems (~4% for Sculptor, ~2% for Fornax using the half-light radius given in McConnachie (2012); ~8% for IC 1613 using the profile fits of Battinelli et al. (2007) to the old populations of the "spheroid"). Statistical studies of TRGB accuracy conclude that approximately 100 stars within one magnitude of the TRGB are necessary to reach the precision necessary for our program (Madore & Freedman 1995; Madore et al. 2009). Thus, we supplement our *HST* data for these objects with a ground-based wide-field campaign using *Magellan*+IMACS, which, with a field of view $>15' \times 15'$, provides a larger area by a factor of 14 for a single pointing. By doing multiple pointings, we can sample the full half-light area for these three objects.

The ground data are "bootstrapped" from the ground-based Johnson-Cousins (i.e., *V* and *I*) system to the native flight magnitude system of *HST* (i.e., $F814W$ and $F606W$). All stars common to the two data sets can be employed for the bootstrapping to ensure appropriate precision is obtained and to investigate for color-terms in the transformation. The magnitude of the TRGB for these galaxies is then determined on the

Table 5
Summary of New Observations Obtained for the TRGB Stage of the CCHP

Target	Class[a]	Supplementary Imaging	R_{gal}	Cepheid Distance?	Notes
TRGB zero-point					
Sculptor	dSph	*Magellan*+IMACS	3.′3 (0.08 kpc)	N	···
Fornax	dSph	*Magellan*+IMACS	6.′2 (0.25 kpc)	N	···
IC 1613	IB(s)m	*Magellan*+IMACS	10.′2 (2.17 kpc)	Y	···
M32	compact E2	···	2.′9 (0.64 kpc)	N	···
M31	SAB(s)b	···	20.′4 (4.62 kpc)	Y	···
M33	dSpr	···	15.′9 (4.08 kpc)	Y	···
SNe Ia zero-point					
M101	SAB(rs)cd	···	11.′6 (23.1 kpc)	Y	SNe Ia: 2011fe
M66	SAB(S)b	···	4.′0 (11.5 kpc)	Y	SNe Ia: 1989B
M96	SAB(rs)ab	···	4.′2 (13.2 kpc)	Y	SNe Ia: 1998bu
NGC 4536	SAB(rs)bc	···	3.′0 (13.4 kpc)	Y	SNe Ia: 1981B
NGC 4526	SAB0(s),edge-on	···	3.′2 (14.2 kpc)	N	SNe Ia: 1994D
NGC 4424	SAB(s)	···	2.′3 (10.3 kpc)	N	SNe Ia: 2012cg
NGC 1448	SAcd, edge-on	···	2.′6 (13.3 kpc)	N	SNe Ia: 2001el
NGC 1365	SB(s)b	···	3.′6 (19.1 kpc)	Y	SNe Ia: 2012fr
NGC 1316	SAB(0) pec	···	9.′2 (53.6 kpc)	N	SNe Ia: 1980D, 1981D, 2006dd, 2006 mr

Note.
[a] From the NASA Extragalactic Database.

photometry of this more populated data set calibrated to $F814W$.

4.3. The Current Error Budget for the TRGB Calibration

The TRGB method has been widely applied and extensively tested by many groups. Most recently, Rizzi et al. (2007) reduced and analyzed in a uniform manner *HST V* and *I* data. Rizzi et al. (2007) find that the mean statistical uncertainty in an individual distance estimate using the TRGB is only 0.05 mag or 2.5% in distance. The geometric distance to the maser host galaxy NGC 4258 has also been measured to an accuracy of 2% in distance, and its TRGB magnitude has also been measured to 2%. Our new seven independent (Local Group and NGC 4258) estimates of the TRGB absolute magnitude will result in an error on the mean of $0.05/\sqrt{7} = 0.019$ mag. For the purposes of understanding our CCHP error budget, we project an error of 0.9% for this stage of the Population II distance ladder.

5. TRGB DISTANCES TO SNE IA HOSTS

The next step in our Population II distance ladder is to calibrate the absolute magnitude for SNe Ia. This is accomplished by applying our TRGB zero-point (Section 4) to TRGB measurements in SNe Ia host galaxies, as we now describe. We discuss the use of SNe Ia for distance measures (Section 5.1), observational concerns over the use of the TRGB (Section 5.2), and estimate our error budget for this step (Section 5.3).

5.1. SNe Ia as Distance Indicators

SNe Ia are the de facto standard candles for determining distances at cosmologically significant scales. SNe Ia, however, are not trivial objects to characterize. Once discovered in transient surveys or by serendipity, the transient event must be typed with spectroscopy, followed with time series and multiband photometry for up to ~30 days to identify maximum light from which the proper decline rate correction is determined, and a long-baseline photometry is required to determine a precise host galaxy template from which the internal component of reddening can be estimated (see Hamuy et al. 2006, for a good description of the required data for SNe Ia characterization). The need for such studies to be undertaken with as few systematics as possible has inspired several large-scale SNe Ia surveys, including the CSP (see Freedman et al. 2009; Folatelli et al. 2010; Burns et al. 2014, for descriptions of the process).

The internal scatter (i.e., the precision) of SNe Ia luminosities is found to be ~0.16 mag (e.g., Folatelli et al. 2010). SNe Ia are intrinsically rare events, and it is even more unusual to have one occur sufficiently close to the Milky Way that the distance to its host galaxy can be independently measured. In the last quarter century there have been only 19 SNe Ia found and measured (using modern, linear detectors) in spiral galaxies that are close enough for their distances to be determined independently by Cepheids.[16]

Beyond the limited sample size, there are other concerns with respect to the SNe Ia. In particular, there is evidence (e.g., Sullivan et al. 2010; Rigault et al. 2015, among others) that the absolute magnitudes of SNe Ia depend on whether they are hosted by lower mass (spiral and/or irregular) or high-mass (elliptical and/or lenticular) galaxies. The Cepheid distance scale is only applicable to SNe Ia whose hosts contain significant young (20–400 Myr) populations, predominantly spiral galaxies. Thus, a Cepheid-based calibration of the SNe Ia absolute magnitude is subject to any population effects within the SNe Ia sample (regardless of whether systematic or random in nature). Our Population II route will immediately bring SNe Ia hosted by non-spiral systems into the calibration sample and provides a direct test of such population differences. Additionally, the use of Population II distance indicators permits use of SNe Ia in host galaxies where the

[16] We note that 11 of these 19 galaxies were presented in Riess et al. (2016) for the first time.

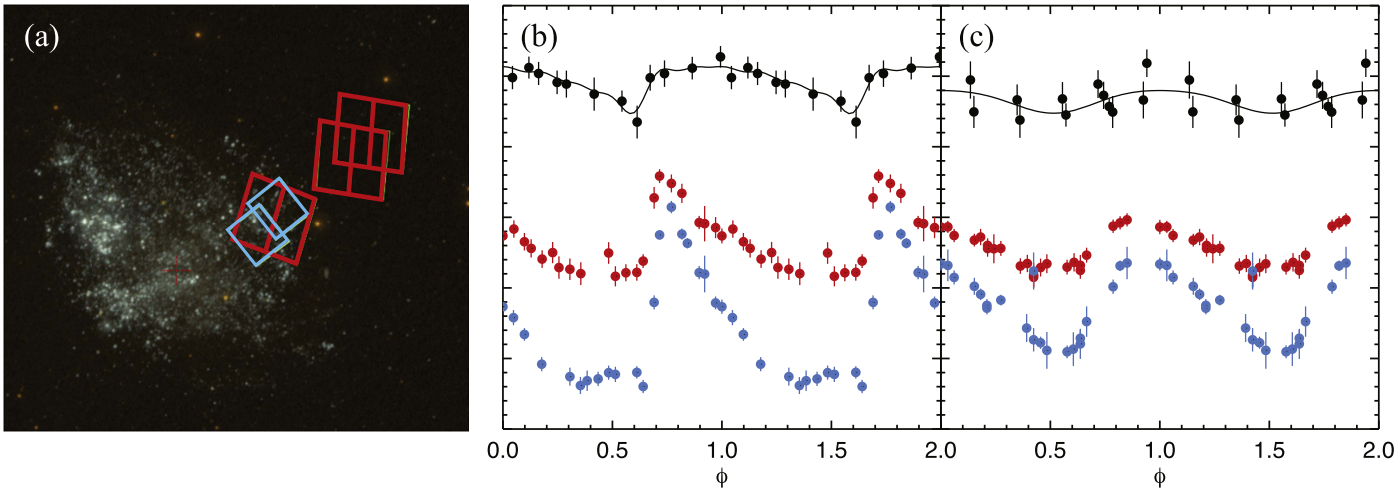

Figure 6. Example Local Group RR Lyrae and TRGB data for IC 1613. (a) Image demonstrating our *HST* + WFC3–IR RR Lyrae and *HST* + ACS TRGB observations from the LCID project (inner fields) and our ACS parallel fields in the inner halo of IC 1613 (outer fields). The background image is from *GALEX*. Example light curves for (b) a type RRab (V039) with a period of 0.520 days and for (c) a type RRc (V130) with period 0.314 days (D. Hatt et al. 2016, in preparation). Sample *HST* light curves in the optical ($F475W$, blue, bottom; $F814W$, red, middle Bernard et al. 2010), and NIR ($F160W$, black, top; D. Hatt et al. 2016, in preparation). As a part of this program, we derive new photometry for the literature data, but adopt the period measurements from earlier discovery work. The black line shows the best-fit *HST* NIR imaging template via Yang & Sarajedini (2012).

Cepheid population is not suitable because of crowding or large extinction, as occurs commonly for edge-on galaxies.

Regardless of Hubble type, galaxy luminosity, and inclination, hundreds of TRGB stars populate the dust-free, low-metallicity, low-crowding stellar halos. Nine SNe Ia have been found in such galaxies in the past quarter century; all but one of them had good-quality (non-photographic) light curves. The TRGB is not without pitfalls, however, the most important of which is the need to choose pointings appropriate for the method to reliably produce measurements of the quality required here.

5.2. Choice of Fields for the TRGB Method

Before discussing the calibration of the TRGB further, there are several challenges of the TRGB as a distance indicator that are worth consideration in the development of a Population II distance scale. Two important examples of applying the TRGB method inappropriately are M101 and NGC 4038/39. As we will discuss in application to these two case studies, there are clear reasons, either in the observational data or in the edge-detection itself, that drive the dispersion in published distance estimates.

There are four published TRGB distance estimates to M101 in the literature: they range from 29.05 ± 0.06 (random) ±0.12 (systematic) mag (Shappee & Stanek 2011), to 29.42 ± 0.04 (random) ±0.10 (systematic) mag (Sakai et al. 2004), to 29.34 ± 0.08 (random) ±0.02 (systematic) mag (Rizzi et al. 2007), and then most recently a value of 29.30 ± 0.01 (random) ±0.12 (systematic) mag (Lee & Jang 2012) based on the weighted mean of nine individual fields. These studies present a wide range of moduli, spanning almost 0.4 mag (in contrast, the Cepheid-based distances span a range of 0.7 mag, see the compilation in Lee & Jang 2012). Not only do the cited distances span a wide range, but this sample demonstrates the broad range of uncertainties quoted (both random and systematic) by various studies.

As it stands, this is an unacceptable outcome for ultimately calibrating the SN Ia. Unfortunately, the fields used to determine the TRGB distances were based on the same data used to study the Cepheids. Owing to their initial purpose, all of those fields are well into the disk of M101 and are therefore very crowded at the significantly fainter magnitude level of the TRGB. Moreover, they are heavily contaminated by brighter intermediate-age AGB and post-AGB stars that confuse and bias any attempt(s) to identify a pure sample of TRGB stars in the optical bands.

This latter problem and its negative consequences are not new. Saviane et al. (2004, 2008), using data deep into the star-forming regions of NGC 4038/39 and contaminated by a brighter and dominant population of AGB stars, measured the distance moduli to be $\mu = 30.7 \pm 0.25$ (random) ± 0.14 (systematic) mag and $\mu = 30.62 \pm 0.09$ (random) ±0.14 (systematic) mag, respectively. This was soon rectified by Schweizer et al. (2008), who measured the TRGB at $\mu = 31.51 \pm 0.12$ (random) ± 0.12 (systematic) mag. This measurement pushed the host galaxy out to 20.0 Mpc, nearly a 50% increase over the distance of 13 Mpc suggested by the initial studies. More recently, Jang & Lee (2015) have independently confirmed the result of Schweizer et al. (2008). Again, high-quality distances can be determined if proper care is taken to either avoid the high stellar density disk or to systematically exclude crowded regions from the TRGB fit.

Further confirmation of the importance of carefully selecting TRGB halo fields comes from the complementary studies of Caldwell (2006) and Durrell et al. (2007), each of which used *HST*+ACS to measure TRGB distances to individual Virgo cluster dwarf galaxies, and in Caldwell (2006), to intra-cluster stellar populations. These observations were designed with the TRGB in mind and targeted regions of low stellar density with limited contamination from young and intermediate-age populations. A mean distance modulus of $\mu = 31.05 \pm 0.05$ mag or $d = 16.1 \pm 0.4$ Mpc was obtained for the nine fields (seven dwarfs and two intermediate regions). Individual distance moduli have quoted uncertainties of ∼0.10 mag and span a range of 0.3 mag. We note, however, that identical methods and data-collection strategies were used in these works, and confirmation by an independent team (as was the case for M101 and NGC 4038/39) is required to verify these measurements. Nevertheless, as was shown for NGC 4258 in

Figure 5 and as has been demonstrated in the literature for M66 and M96 (Lee & Jang 2013), M74 (Jang & Lee 2014), and NGC 5584 (Jang & Lee 2015), in addition to these previously described objects, halos provide excellent environs for application of the TRGB as a distance indicator.

In the cases where the TRGB is measured using imaging of appropriate galactic locales, i.e., those in which the old metal-poor population dominates, and in which careful consideration is given to how to measure the discontinuity, the TRGB proves to be of comparable precision as other distance indicators at these faint magnitudes.

5.3. The SNe Ia Zero-point Error Budget

In our sample, there are 9 galaxies that have hosted 12 well-observed SNe Ia (Table 5), with the most distant object, NGC 1316, hosting 4 SNe Ia. Our observing strategy for these galaxies was based on the study of Caldwell (2006), who measured the TRGB for the equally distant Virgo cluster dwarfs with ACS to a precision of 0.1 mag. However, we adopt the much higher throughput filter $F606W$, as opposed to $F555W$ as used by Caldwell (2006), to increase observing efficiency. The *HST* observations (Table 5) were designed to yield a 10σ detection at the TRGB in the $F814W$ filter and, since the color will only be used to remove contaminants, a $\sim 3\sigma$ detection in $F606W$ for stars at the anticipated TRGB in each galaxy. Preliminary reductions of one of our more distant objects, NGC 1365, to be presented by I. Jang et al. (2016, in preparation), suggests this goal for the signal-to-noise ratio is being met.

The field choice for our *HST* imaging was governed by the following general strategy. First, we avoided extended disks and other obvious young or tidal structures. Second, we attempted to target preferentially along the minor axis to minimize the likely contamination from low surface-brightness thick-disk structure. Lastly, we straddled the *WISE* W1 25–26 mag arcsec^{-2} isophote, and if applicable, the *GALEX* Near-UV 27–28 mag arcsec^{-2} isophote (using custom builds of the public raw data). This resulted in a sample that ranges in galacto-centric distances from ∼10 kpc in NGC 4424 (one of the least luminous galaxies) to ∼60 kpc in NGC 1316 (having prominent shell features and being one of the most massive galaxies). The total anticipated RGB source density was confirmed using published data from Mager et al. (2008) for NGC 4258 and from Lee & Jang (2013) for M66 and M96, as well as providing verification of our signal-to-noise ratio estimates.

Using the metallicity profile of Gilbert et al. (2014) for the resolved stellar halo of M31 (between $R_{\rm proj} \sim 10$ and 165 kpc) as a proxy for our galaxies, we can expect an M31-analog galaxy to have median stellar metallicities between ~ -0.5 dex and ~ -1.0 dex over this radius range (see Figure 11 of Gilbert et al. 2014). The dispersion of the median metallicity is ∼0.5 dex at any given location (see Figure 9 of Gilbert et al. 2014). Thus, the range of metallicities we expect in our SNe Ia hosts is representative of the range of [Fe/H] spanned by our Local Group and Galactic targets (Table 4). Thus, our TRGB ZP determination relative to the RRL will include variations over this metallicity range.

A great benefit of the metallicity dependence of the TRGB is that, unlike the dependence for RRL and Cepheids, the effect of metallicity is encoded into the color of the RGB star, and the most metal-poor stars—those that dominate in our halos—are brighter than the metal-rich stars. Thus, adding additional metal-rich stellar populations will "blur" the tip detection preferentially to fainter magnitudes. The total impact on our TRGB measurements will depend on the star formation history of a given pointing, and we can use our M31, M33, and M32 TRGB data to study these effects empirically within the context of our program. For the purposes of this discussion, we assume an equal distribution of stars over our color range. The impact of metallicity on the TRGB detection has been studied by Rizzi et al. (2007), Mager et al. (2008), and Madore et al. (2009, among others), and these studies consistently find a TRGB slope of ∼0.2 mag color^{-1} for both the ground-based Johnson filters and the *HST* flight magnitude system. Using the published TRGB results of Lee & Jang (2013), we can expect a well populated TRGB over a 0.5 mag color range in $F606W - F814W$, which implies a uniform change in the TRGB magnitude of ∼0.1 mag in $F814W$ (using the TRGB slope in the flight magnitude system from Rizzi et al. 2007). Converting the uniform change into an effective dispersion, we predict a blurring over this color range of $\sigma_{\rm [Fe/H]} = 0.028$ mag.

Taking considerations from the previous sections to heart, as part of our program, we plan to reanalyze the Lee & Jang (2013) pointings for M96 and M66 (GO-10433), as well as extensive archival fields (taken as parallel pointings) available for NGC 4258 and M101 that reach a similar signal-to-noise ratio as our primary program. This will provide independent checks on our methods (i.e., in comparison to previous work) and also direct empirical tests for AGB-contamination, crowding, and metallicity effects as a function of galacto-centric radius for these objects.

For our final measurement of H_0 from this distance ladder, individual fitting errors, derived independently for each galaxy and including constraints on the effects of metallicity (color), crowding, and completeness, will be used (a first exploration of this will be presented for NGC 1365 by I. Jang et al. 2016, in preparation). For the goals of this work, we make an estimate of the uncertainty for the CCHP error budget by adopting twice the TRGB fitting uncertainty from Rizzi et al. (2007) ($\sigma = 0.10$ mag) to account for increased errors in the *I*-band photometry at the tip for our more distant sample of SNe Ia hosts, a value that is consistent with the uncertainties quoted by Caldwell (2006) for the Virgo cluster. We adopt a TRGB blurring of $\sigma_{\rm [Fe/H]} = 0.028$ mag, which is negligible when added in quadrature to our anticipated TRGB fitting uncertainty. To our total TRGB uncertainty, we then add in quadrature the 0.12 mag intrinsic scatter in the SNe Ia absolute magnitudes (with the term for large-scale flows removed, see Folatelli et al. 2010) and obtain a projected uncertainty for our calibrating sample of ±0.157 mag per source. For the pure Population II calibration using twelve TRGB-calibrated SNe Ia, we obtain a systematic error on the mean of $0.157/\sqrt{12} = 0.046$ mag or 2.1% in distance. Thus, we project a 2.1% uncertainty for this stage of the distance ladder.

6. INTO THE HUBBLE FLOW

Given a larger sample of SNe Ia calibrating galaxies, augmented by SNe Ia calibrated by Population II distance indicators, directly traceable to parallaxes, we will derive a new value of H_0 based on several hundred SNe Ia at distances well into the smooth Hubble flow. Well-observed light curves for these SNe Ia can be directly adopted from CSP1 (Stritzinger et al. 2011, and references therein), CfA4 (Hicken et al. 2012, and references therein), Pan-STARRS1 (Rest et al. 2014, and references therein), and CfAIR2 (Friedman et al. 2015, and

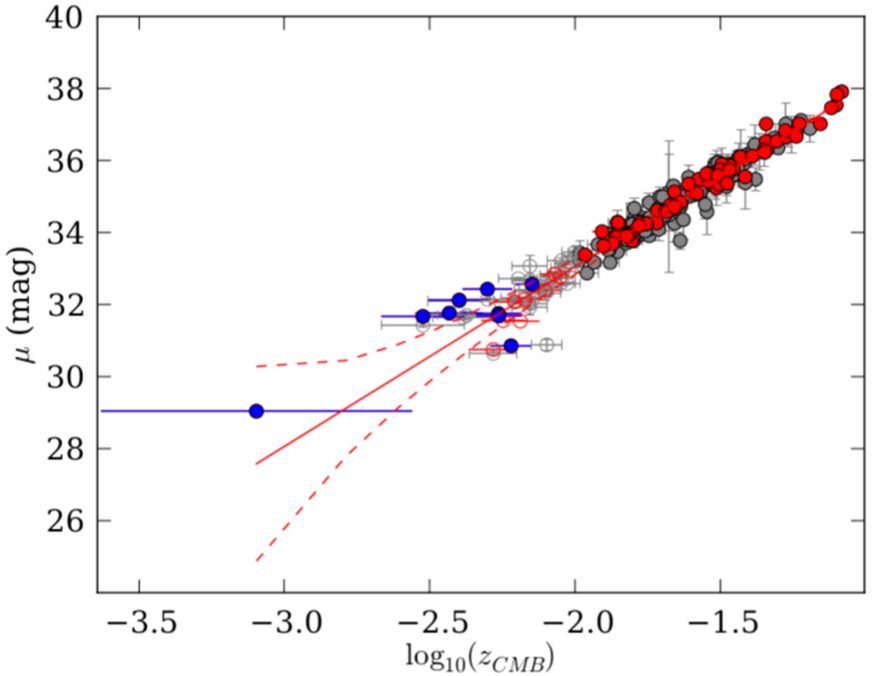

Figure 7. Illustrative SNe Ia Hubble diagram comparing the distance modulus and redshift for SNe Ia. Gray symbols are data from the literature (primarily from the CfA4 data release, Hicken et al. 2012). Red symbols are those supernovae included in the CSP-1 (e.g., Stritzinger et al. 2011). Blue symbols are the local supernova calibrators, demonstrating the larger scatter induced by local large-scale flows for nearby objects.

references therein). Conservative selection of low-z SNe Ia with low internal extinction from these data releases suggests that approximately 221 suitable objects are available now. By the completion of our program, we anticipate additional SNe Ia light curves to be released, both from additional data released from the more recent incarnations of the CSP and CfA programs and from the continued operations of Pan-STARRS (*The Foundation Survey*; R. Foley 2016, private communication), the Dark Energy Survey, and other large-area, multiepoch imaging programs.

Figure 7 is a Hubble diagram that uses data from CfA4 (Hicken et al. 2012) and the CSP1 (Stritzinger et al. 2011) to demonstrate this last step in our distance ladder (we note this is not the full sample available now in the literature). Figure 7 contains 130 SNe Ia from CSP (red and blue points) and 94 from CfA4 (gray). The SNe Ia presented in Figure 7 were selected to have both had first epoch observations within 10 days post maximum and with light-curve stretch factors less than 0.5 (i.e., fast decliners are excluded) for a total of 215 objects with redshifts higher than 0.1 (64 objects were from CSP). The CSP SNe Ia were observed in the near-IR, which has two benefits: decreased extinction and decreased decline rate corrections (for details, see the review by Phillips 2012). This improves the resulting measurements (compare the variance of the red and gray points in Figure 7). By the conclusion of our program, we anticipate Figure 7 to have evolved significantly with the continued operations of the previously described SNe Ia characterization programs.

This final step in the Population II distance scale is probably the most secure in its precision and accuracy given the small scatter of the SNe Ia that are safely in the Hubble flow ($\sigma = 0.16$ mag Folatelli et al. 2010). At the same time, Figure 7 also demonstrates the large scatter in the "local" SNe Ia sample calibrated to Cepheids (blue points), whose line-of-sight motions have a higher fractional impact from their peculiar motions. The variance shown in Figure 7 will only improve with the ongoing projects to better quantify the Hubble flow.

Using a representative sample (i.e., Figure 7), we can estimate the precision afforded by this stage of the CCHP distance ladder. A dispersion of 0.16 mag for SNe Ia around the Hubble line (Folatelli et al. 2010) gives, for a sample of 221 low-z and low-reddening SNe Ia hosts, a negligible error on the mean of only $0.16/\sqrt{221} = 0.011$ mag. We note that the number of SNe Ia will only increase over the progression of the CCHP. The dispersion estimate from Folatelli et al. (2010) already includes the uncertainty arising from averaging over large-scale flows (~0.5%; Riess et al. 2009). At this stage of our program, we anticipate a final combined error of 0.5%.

7. DISCUSSION AND FUTURE WORK

The CCHP will provide a test of the Cepheid-based distance ladder with an equally (or more) precise and systematically independent distance scale. We will produce an end-to-end calibration of the RR Lyrae distance scale in $F160W$. Coupled with TRGB distances outside of the Local Group, the CCHP allows for a new and robust determination of the Hubble constant. In this section, we review our error budget (Section 7.1) and discuss future improvements for the calibration of the zero-points for the RRL PL relation (Section 7.2), TRGB (Section 7.3), and SNe Ia (Section 7.4), and their impact on the measurement of H_0.

7.1. Summary CCHP Error Budget

We now summarize the uncertainties for each of the steps in our current Population II distance ladder, as given in the black notation in the top fork of Figure 8. The CCHP has a geometric foundation calibrated by five Galactic RR Lyrae with *HST*+-*FGS* parallaxes (Section 3), which calibrate the zero-point of the RRL $F160W$ PL relation to 1.7% (first box in top fork of

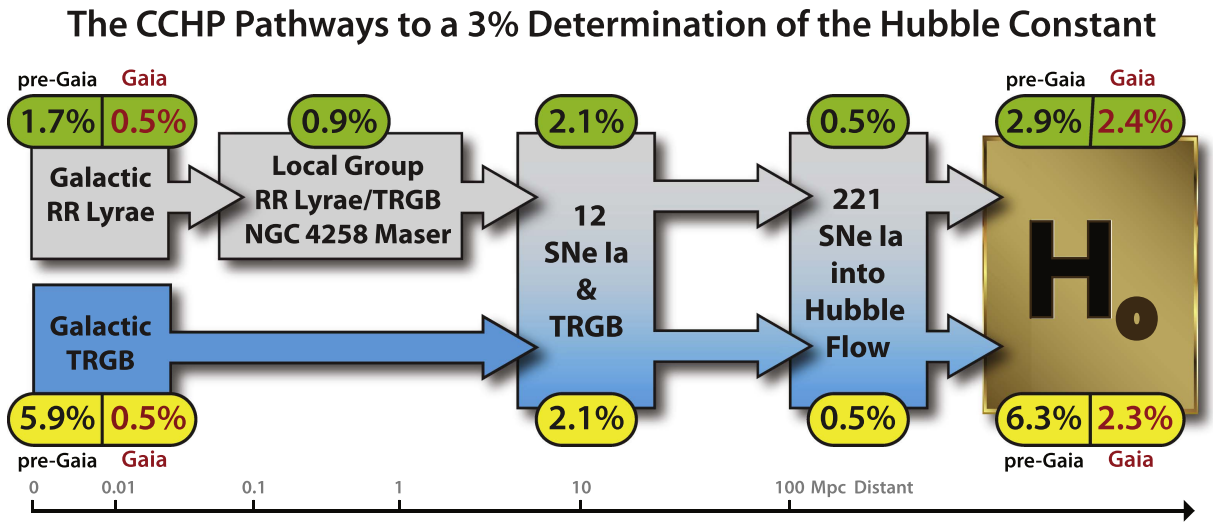

Figure 8. Schematic representation of the projected error budget for H_0 with only Population II distance indicators, using the conservative estimates described in the text, where the current budget is given in black text and the projected budget after *Gaia* is in red text. Two paths are given; the first is the one described in the text that uses RR Lyrae to calibrate the TRGB and the TRGB to calibrate the SNe Ia (top fork), and the second is a path that calibrates the TRGB directly and then uses the TRGB to calibrate the SNe Ia (bottom fork). The scale bar at the bottom of the figure gives the approximate line-of-sight distance scale in units of Mpc for the measurements taken at each step of the Population II distance ladder. (Top fork) Illustration of the current CCHP distance ladder using the 5 trigonometric parallaxes with *HST*+*FGS*, resulting in a 2.9% measure of H_0 (Section 7.1). Projected CCHP distance ladder error budget using ~55 trigonometric parallaxes from *Gaia*, resulting in a 2.4% measure of H_0 (Section 7.2). (Bottom fork) Projected CCHP distance ladder bypassing the RR Lyrae and using the *Hipparcos* parallaxes for local TRGB stars, resulting in a 6.3% measure of H_0 (Section 7.3). Projected CCHP distance ladder using only the TRGB stars, but with improved *Gaia* parallaxes, resulting in a 2.3% measure of H_0 (Section 7.3). Despite minimizing the distance ladder and substantially reducing uncertainties, the number of SNe Ia zero-point calibrators sets the floor on the "local" measurement of H_0 at 2.1%.

Figure 8). The megamaser distance to NGC 4258 and RRL in six Local Group galaxies provide seven independent calibrations of the zero-point for the TRGB (Section 4) to 0.9% accuracy (second box in top fork of Figure 8). The TRGB is then used to set the zero-point for the local SNe Ia sample, here in a set of 9 host galaxies with a total of 12 individual SNe Ia (Section 5), resulting in a precision of 2.1% (middle box of Figure 8). The CCHP can then tie into the current sample of over 200 (and growing) well-observed SNe Ia well into the Hubble flow (Section 6) with a precision of 0.5% (second box from right in Figure 8). Combining in quadrature each of the four systematic uncertainties in the Population II route to the Hubble constant, we conclude that a net uncertainty of 2.9% is achievable with this program (rightmost box for the top fork of Figure 8).

An ancillary benefit of CCHP is the ability to compare this distance ladder to that from the Cepheids. As indicated in Table 5, five galaxies in our SNe Ia sample and three in our Local Group sample also have distances via the Leavitt Law and, often, measured by multiple independent teams (see summary in Freedman & Madore 2010b; Freedman et al. 2012b). Thus, we can look for effects that are due to crowding, reddening, and metallicity in the Cepheid distances by comparing their results with those from this program (see discussion in Section 1.1). Moreover, we gain additional leverage on the calibration of the SNe Ia zero-point by combining host galaxies with distances determined from both Population I and Population II distance indicators, although this is a process that requires extreme care as it combines measurements with very different systematic uncertainties. Thus, we anticipate that the greatest gain from the existence of two independent distance ladders is the ability to test individually stages of either distance ladder with a careful and systematic approach. In the near future, however, there are significant opportunities to improve stages of these two distance ladders (although we focus in the following discussion on the Population II route described here).

7.2. *Gaia* Parallaxes for RR Lyrae Variables

As summarized in Clementini (2016, and references therein), *Gaia* is expected to observe over 100,000 Galactic RRL, a sample increase of several orders of magnitude compared to the 186 observed by *Hipparcos*. According to *Gaia*'s post-commissioning performance estimates (see Table 1 in de Bruijne et al. 2014), all RRL with $\langle V \rangle < 12.1$ mag will have the parallax measured to better than ~10 μas, whereas individual accuracies will range between 17 and 140 μas for RRL in Galactic globular clusters with typical $\langle V_{HB} \rangle$ between 14 and 18 mag. This implies that in a few years there will be more than an order of magnitude more RRL PL zero-point calibrators. Moreover, owing to improvements in period coverage and metallicity spanned by this larger sample, it may even be feasible to calibrate all terms in the PL–metallicity relation directly from the calibrators.

According to the current plan[17], with the first *Gaia* release having occured in September 2016, parallaxes with submilliarcsecond accuracy for the stars in common between the Tycho-2 Catalog and *Gaia* will be available soon. This initial catalog will be based on the Tycho-*Gaia* Astrometric Solution (TGAS; see Michalik et al. 2015) that will compare positions between the *Gaia* first release and the Tycho-2 catalog. Folding the *Gaia* trigonometric parallaxes into our Population II distance scale, however, requires additional observations.

In anticipation of the parallaxes being obtained by *Gaia*, we are obtaining high-quality *B*, *V*, *I* optical light curves of the quality demonstrated for RR Gem in Figures 3(a) and (b) for 55

[17] The release plans are available here: http://www.cosmos.esa.int/web/gaia/release.

Galactic RRL with the Three-hundred Millimeter *Magellan* Telescope (TMMT; A. Monson et al. 2016, in preparation). A completed *HST* Cycle 21 SNAP program to obtain *F*160*W* magnitudes includes 25 additional Galactic RRL calibrators (PID 13472 Freedman 2013) for a total sample of 30 such stars when combined with the CCHP presented in Section 3.1.1. These same 55 stars were also included in the CRRP (Freedman et al. 2012a, V. Scowcroft et al. 2016, in preparation) and have light curves in the MIR similar to that of RR Gem in Figure 3(d). When the trigonometric parallaxes become available, these additional Galactic calibrators can be seamlessly folded into the framework described in Section 3 to set the RRL foundation for the CCHP.

Beyond the gains for the Galactic calibrators, *Gaia* will also provide distances to better than 1% for about 77 Galactic globular clusters (49% of the known clusters and all clusters within 16 kpc; Cacciari 2013). Thus, *Gaia* will directly probe the RRL population within ω Centauri and other clusters within ~16 kpc of the Sun. When coupled with chemical abundances derived from high-resolution spectroscopy, the larger sample of RRL within *Gaia* has the potential to resolve concerns over how metallicity affects the PL, both for the slope and zero-point (i.e., discussions in Section 3.2), which will further reduce the uncertainty associated with the use of RRL.

The order-of-magnitude increase in parallax calibrators and the more than an order-of-magnitude decrease in mean parallax error could drop the uncertainty on the RRL zero-point from 1.7% to 0.5% in distance ($0.079/\sqrt{55} = 0.011$ mag; indicated by red text in the leftmost box in upper fork of Figure 8; note that we have adopted the zero-point fitting uncertainty from Section 3.1.1 as an upper limit). Propagating this change through to the measurement of H_0 reduces the total predicted uncertainty on H_0 from 2.9% to 2.4% (indicated by red text in the rightmost box in the upper fork of Figure 8).

7.3. Bypassing the RR Lyrae Variables

As previously discussed, the current systematic error on the absolute TRGB magnitude is 0.12 mag or 6% in distance (Rizzi et al. 2007) and thus going directly to the TRGB at present is not an improvement from our current two-step process using the RRL (black notations in the forks of Figure 8). Moreover, using the current TRGB calibration results in a 6.3% measure of H_0 that is not currently competitive with our current path (~3.0% measure of H_0). Ultimately, if we wish to calibrate the TRGB directly to better than 1%, we must construct a distance ladder that relies only on the TRGB technique from our local environment that is then applied directly to the SNe Ia calibrators.

Tabur et al. (2009) have combined *Hipparcos* (Perryman et al. 1997) and photometry from the 2-Micron All Sky Survey (2MASS Skrutskie et al. 2006) to calibrate the magnitude of the TRGB in the NIR (K_s). An optical all-sky catalog with comparable photometric precision does not yet exist. Following the example of Tabur et al. (2009), we are producing high-quality optical photometry for as many tip stars as are accessible from Las Campanas Observatory. More than 1000 of the Tabur et al. (2009) tip stars (determined from *Hipparcos*) are accessible by the TMMT, and we are pursuing *B*, *V*, *I* photometry for these stars (with multiple epochs to test for variable AGB contaminants at the tip).

The current CCHP TMMT sample contains over 1000 stars, and the resulting TMMT *I*-band magnitudes (part way through the survey) have mean photometric error of $\sigma_I \sim 0.04$ mag (with removal of stars showing variability). Unfortunately, the current *Hipparcos* parallaxes have a mean $\sigma_\pi/\pi = 30\%$, and the average M_I is only accurate to $\sigma_{M_I} \sim 0.9$ mag or 45% in distance. Conservatively assuming ~50 bona fide tip stars, this results in an uncertainty of 0.128 mag (5.9% in distance), which offers no improvement on prior isochrone-based TRGB calibrations (Section 4).

The median magnitude of our TRGB sample is $I = 5.34$ (the average is $\langle I \rangle = 7.4$), which also falls well within the highest precision *Gaia* sample ($\sigma_\pi < 7$ μas for $3 < G < 12.1$ mag; see de Bruijne et al. 2014, for end of mission values). Assuming the fractional error of the trigonometric parallaxes (π) is reduced tenfold for our sources (a conservative projection), the mean $\sigma_\pi/\pi = 3\%$. Using our mean *I* magnitude error ($\sigma_I = 0.04$) and a conservative estimate of 50 stars at the tip, *Gaia* produces a 0.5% calibration of the TRGB magnitude. *Gaia* will sample many more tip stars than *Hipparcos* and with corresponding optical photometry can be added to our calibration sample (e.g., Mignard 2003, 2005). Moreover, the associated spectroscopic data products ($R = 11{,}500$) from *Gaia* for stars brighter than $G \sim 16$ will permit a high-precision *empirical* calibration of the metallicity dependence that is fully empirical and relies on metallicities derived from a homogeneous analysis (i.e., not using isochrones as in previous calibrations by Mager et al. 2008; Madore et al. 2009).

Using projections for a *Gaia* calibration of the TRGB, we estimate that a 2.6% measure of H_0 is feasible (rightmost box of the bottom fork of Figure 8). The *Gaia* branch of the bottom fork of Figure 8 represents a route to H_0 where the floor set by the uncertainty on the SNe Ia zero-point is reached. Upon the completion of the work described here, the number of SNe Ia calibrators (i.e., those near enough for independent distance determination) becomes the single limiting factor in the "local" measure of H_0.

7.4. The SNe Ia Calibrator Sample

Even anticipating the significant gains for the distance ladder provided by the *Gaia* parallaxes, the total H_0 error budget is driven by the relatively small number of local SNe Ia calibrators (see blue points in Figure 7). More importantly, this step affects not just our Population II route, but also those using Cepheids (e.g., SH_0ES and CHP; Riess et al. 2011; Freedman et al. 2012b). As discussed by Freedman & Madore (2010b), the small number of SNe Ia calibrators is a function of several factors: (i) nature's rate of SNe Ia production, (ii) the ability of the astronomical community to detect transient objects, and (iii) the properties of the host galaxy that make the SNe Ia an ideal calibrator. While we have no control over the rate of SNe Ia, the CCHP Population II distance ladder now permits using SNe Ia that are found in early-type and in edge-on late-type host galaxies, which would previously have been precluded from the calibrator sample owing to limitations of distance measurements with Cepheids. Detectability of SNe Ia can only be improved with the increased number and efficiency of transient surveys, for example, the dual-hemisphere ASAS-SN (e.g., Shappee et al. 2014) and the full-sky multiepoch monitoring provided by the *Gaia* satellite (with alerts predicted to total over 6000 transient objects over its five-year lifetime), which permit a vastly more complete sample of nearby bright SNe Ia to be discovered.

These discoveries can only be capitalized upon for the distance ladder under specific circumstances, which are that the host galaxy is amenable to the non-trivial SNe Ia follow-up described in Section 5 and within the volume probed by independent distance measures. There are two factors setting volume: (i) collecting area (aperture), and (ii) resolution. For *HST*, this volume (set by practical concerns) is ∼35 Mpc for Cepheids, ∼20 Mpc for the optical TRGB, and ∼1 Mpc for the optical/NIR RR Lyrae—all of which require large numbers of orbits (>10 orbits, with the non-variable TRGB being the most overall observationally efficient). With a sevenfold increase in collecting area and a fourfold increase in resolution, the *James Webb Space Telescope* will greatly extend the volume within SNe Ia host galaxies that have independently determined distances. Proposed 30 m class optical telescopes equipped with adaptive optics, such as the Giant Magellan Telescope, the Thirty-Meter Telescope, and the European Extremely Large Telescope will be able to surpass *HST* resolution in the NIR and will boast at minimum a 150-fold increase in collecting area over *HST*, although these gains will be modulated by atmospheric conditions. The combination of an increased observational effort from transient surveys, the new large-aperture and high-resolution facilities, and the ability to follow-up SNe Ia from nearly any host galaxy using our Population II techniques, demonstrates that the technology and infrastructure are available to increase the number of SNe Ia calibrators.

The fiducial precision required to place high-level constraints on the CMB modeling from these "local" techniques is to measure H_0 to 1% (see discussions in Planck Collaboration et al. 2014). When we use the minimal Population II ladder that is schematically visualized in the bottom fork of Figure 8 with a *Gaia*-calibrated TRGB and no other changes to the method, reaching 1% in H_0 would require a SNe Ia zero-point calibrated to 0.7% and would require ∼100 SNe Ia calibrators. With 50 SNe Ia calibrators, the SNe Ia zero-point is calibrated to 1.5% and H_0 measured to 1.7%; with 25 SNe Ia calibrators, the zero-point is calibrated to 0.9% and H_0 to 1.3%. We estimate that the anticipated number of nearby SNe Ia is severely limited by Poisson noise (and the relatively short operational lifetimes of all-sky transient programs—1–2 years; Holoien et al. 2016), but a "handful" (two to five) can be anticipated on an annual basis (Gal-Yam et al. 2013).[18] Thus, it may be feasible in the next two decades to reach a ∼1% measure of H_0 from the Population II distance ladder.

8. FINAL REMARKS

The goal of the CCHP is to measure H_0 using a distance ladder constructed only from Population II distance indicators. Initially, the ladder will contain three distance tracers: the NIR RRL PL within 1 Mpc, the optical TRGB within ∼20 Mpc, and the SNe Ia well into the smooth Hubble flow. This path to H_0requires calibrating the $F160W$ PL for RRL and providing a high-precision calibration of the TRGB zero-point, however. Using reasonable estimates for our error budget (i.e., upper limits on individual measurements), this four-step ladder (top fork in Figure 8) could initially provide a 2.9% measure of H_0 with data available at the present time.

While our initial CCHP measure of H_0 is competitive with other distance ladder measures (see compilation in Table 1 and Figure 1), we critically assess how to push the Population II distance ladder to higher precision in the near future. Accounting for improvements to the calibration of the RRL PL relation from *Gaia* (and associated observational campaigns), the H_0 precision attainable from the CCHP distance ladder could improve to 2.4%. Further improvement on the H_0 precision is achieved by bypassing the RRL and using Galactic TRGB calibrators to set the geometric foundation of the Population II scale. With conservative estimates, a TRGB-only distance ladder can approach an H_0 precision of 2.3%, a value that is dominated by the number of independently calibrated SNe Ia.

Resolving the discrepancy between the traditional Cepheid-based distance ladder and CMB modeling remains critical. The CCHP distance ladder is completely independent of the Cepheid distance ladder and as such will provide a systematic check on each stage of the traditional Cepheid ladder. The precision required of the distance ladder measure of H_0 to provide a quantitative assessment of these differences is often set to 1%. Pushing the precision of H_0 to this level is currently hampered by the number of SNe Ia host galaxies with independent distances (Figure 8). With conservative estimates on SNe Ia rates from all-sky transient surveys and the increase in the volume accessible by stellar population distance measures permitted by next-generation facilities, it is possible to achieve such precision within the next few decades.

We thank the anonymous referee for comments that have improved the manuscript. We acknowledge numerous helpful conversations with and insights from Eric Persson. R.L.B. thanks Chris Burns for assistance in making Figure 7 and for helpful discussions on the body of SNe Ia measurements. R.L.B., I.S.J., and B.F.M. also thank the organizers of the *New Era of the Cosmic Distance Scale* summer school at the University of Tokyo for an enlightening exploration of modern distance-measurement techniques and the future of such programs. G.C. wishes to thank Marcella Marconi for discussions on the theoretical background on the luminosity–metallicity and the PL-metallicity relations followed by RR Lyrae in optical and NIR/MIR passbands, respectively. Support for program #13691 was provided by NASA through a grant from the Space Telescope Science Institute, which is operated by the Association of Universities for Research in Astronomy, Inc., under NASA contract NASA 5-26555. G.B. thanks the Japan Society for the Promotion of Science for a research grant (L15518). G.C. acknowledges support by PRIN-INAF2014, Excalibur's: EXtragalactic distance scale CALIBration Using first-Rank Standard candles (P.I. G. Clementini). M.G.L. and I.S.J. were supported by the NRF grant funded by the Korea Government (No. 2012R1A4A1029713). This work is based on observations made with the *Spitzer* Space Telescope, which is operated by the Jet Propulsion Laboratory, California Institute of Technology under a contract with NASA. Support for this work was provided by NASA through an award issued by JPL/Caltech. This research has made use of the NASA/IPAC Extragalactic Database (NED), which is operated by the Jet Propulsion Laboratory, California Institute of Technology, under contract with the National Aeronautics and Space Administration.

Facilities: HST (ACS, WFC3/IR), Magellan: Baade (FourStar), *Spitzer* (IRAC).

[18] Updated daily and available at http://www.rochesterastronomy.org/supernova.html.

REFERENCES

Addison, G. E., Huang, Y., Watts, D. J., et al. 2016, ApJ, 818, 132A
Anderson, L., Aubourg, É., Bailey, S., et al. 2014, MNRAS, 441, 24
Battinelli, P., Demers, S., & Artigau, É. 2007, A&A, 466, 875
Bedregal, A. G., Aragón-Salamanca, A., & Merrifield, M. R. 2006, MNRAS, 373, 1125
Bellazzini, M. 2008, MmSAI, 79, 440
Bellazzini, M., Ferraro, F. R., & Pancino, E. 2001, ApJ, 556, 635
Bellazzini, M., Ferraro, F. R., Sollima, A., Pancino, E., & Origlia, L. 2004, A&A, 424, 199
Benedict, G. F., McArthur, B. E., Feast, M. W., et al. 2011, AJ, 142, 187
Benedict, G. F., McArthur, B. E., Fredrick, L. W., et al. 2002, AJ, 124, 1695
Bennett, C. L., Larson, D., Weiland, J. L., et al. 2013, ApJS, 208, 20
Bernard, E. J., Monelli, M., Gallart, C., et al. 2010, ApJ, 712, 1259
Bersier, D., & Wood, P. R. 2002, AJ, 123, 840
Bevington, P. R., & Robinson, D. K. 2003, Data Reduction and Error Analysis for the Physical Sciences (Boston, MA: McGraw-Hill)
Bono, G. 2003, in Stellar Candles for the Extragalactic Distance Scale, Vol. 635, ed. D. Alloin & W. Gieren (Berlin: Springer)
Bono, G., Caputo, F., Castellani, V., Marconi, M., & Storm, J. 2001, MNRAS, 326, 1183
Braga, V. F., Dall'Ora, M., Bono, G., et al. 2015, ApJ, 799, 165
Burns, C. R., Stritzinger, M., Phillips, M. M., et al. 2014, ApJ, 789, 32
Cacciari, C. 2013, in IAU Symp. 289, RR Lyrae Stars: Prime Calibrators of the First Rung of the Distance Ladder, ed. R. de Grijs (Cambridge: Cambridge Univ. Press), 101
Cacciari, C., & Clementini, G. 2003, in Stellar Candles for the Extragalactic Distance Scale, Vol. 635, ed. D. Alloin & W. Gieren (Berlin: Springer)
Caldwell, N. 2006, ApJ, 651, 822
Cardelli, J. A., Clayton, G. C., & Mathis, J. S. 1989, ApJ, 345, 245
Catelan, M., Pritzl, B. J., & Smith, H. A. 2004, ApJS, 154, 633
Cioni, M.-R. L., Clementini, G., Girardi, L., et al. 2011, A&A, 527, A116
Clementini, G. 2011, in EAS Publications Ser. 45, Pulsating Variable Stars, Powerful Tools for Galactic Structure and Evolution, ed. C. Turon, F. Meynadier, & F. Arenou (London: EDP Sciences), 267
Clementini, G. 2016, arXiv:1602.01104
Clementini, G., Gratton, R., Bragaglia, A., et al. 2003, AJ, 125, 1309
Da Costa, G. S., & Armandroff, T. E. 1990, AJ, 100, 162
de Bruijne, J. H. J., Rygl, K. L. J., & Antoja, T. 2014, in EAS Publications Ser. 67, Gaia Astrometric Science Performance—Post-Launch Predictions, ed. N. A. Walton, F. Figueras, L. Balaguer-Núñez, & C. Soubiraned (London: EDP Sciences), 23
de Grijs, R., Wicker, J. E., & Bono, G. 2014, AJ, 147, 122
Di Valentino, E., Melchiorri, A., & Silk, J. 2015, PhRvD, 92, 121302
Di Valentino, E., Melchiorri, A., & Silk, J. 2016, PhLB, 761, 242
Dunkley, J., Komatsu, E., Nolta, M. R., et al. 2009, ApJS, 180, 306
Durrell, P. R., Williams, B. F., Ciardullo, R., et al. 2007, ApJ, 656, 746
Efstathiou, G. 2014, MNRAS, 440, 1138
Eisenstein, D. J., Zehavi, I., Hogg, D. W., et al. 2005, ApJ, 633, 560
Eyer, L. 2000, in ASP Conf. Ser. 203, IAU Coll. 176: The Impact of Large-Scale Surveys on Pulsating Star Research, ed. L. Szabados & D. Kurtz (San Francisco, CA: ASP), 41
Feast, M. W., Laney, C. D., Kinman, T. D., van Leeuwen, F., & Whitelock, P. A. 2008, MNRAS, 386, 2115
Fiorentino, G., Contreras Ramos, R., Tolstoy, E., Clementini, G., & Saha, A. 2012, A&A, 539, A138
Folatelli, G., Phillips, M. M., Burns, C. R., et al. 2010, AJ, 139, 120
Freedman, W. 2013, The Hubble Constant to 1%? STAGE 4: Calibrating the RR Lyrae PL Relation at H-Band using HST and Gaia Parallax Stars HST Proposal
Freedman, W. 2014, CHP-II: The Carnegie Hubble Program to Measure Ho to 3% Using Population II, HST Proposal
Freedman, W., Madore, B., Mager, V., et al. 2008, The Hubble Constant, Spitzer Proposal
Freedman, W., Scowcroft, V., Madore, B., et al. 2012a, The Carnegie RR Lyrae Program, Spitzer Proposal
Freedman, W. L. 1988, AJ, 96, 1248
Freedman, W. L., Burns, C. R., Phillips, M. M., et al. 2009, ApJ, 704, 1036
Freedman, W. L., & Madore, B. F. 2010a, ApJ, 719, 335
Freedman, W. L., & Madore, B. F. 2010b, ARA&A, 48, 673
Freedman, W. L., & Madore, B. F. 2011, ApJ, 734, 46
Freedman, W. L., Madore, B. F., Gibson, B. K., et al. 2001, ApJ, 553, 47
Freedman, W. L., Madore, B. F., Scowcroft, V., et al. 2012b, ApJ, 758, 24
Friedman, A. S., Wood-Vasey, W. M., Marion, G. H., et al. 2015, ApJS, 220, 9
Gal-Yam, A., Mazzali, P. A., Manulis, I., & Bishop, D. 2013, PASP, 125, 749
Gilbert, K. M., Guhathakurta, P., Beaton, R. L., et al. 2012, ApJ, 760, 76
Gilbert, K. M., Kalirai, J. S., Guhathakurta, P., et al. 2014, ApJ, 796, 76
Gratton, R. G., Tornambe, A., & Ortolani, S. 1986, A&A, 169, 111
Grocholski, A. J., Cole, A. A., Sarajedini, A., Geisler, D., & Smith, V. V. 2006, AJ, 132, 1630
Hamuy, M., Folatelli, G., Morrell, N. I., et al. 2006, PASP, 118, 2
Harris, W. E. 1996a, AJ, 112, 1487
Harris, W. E. 1996b, yCat, 7195
Herrnstein, J. R., Moran, J. M., Greenhill, L. J., et al. 1999, Natur, 400, 539
Hicken, M., Challis, P., Kirshner, R. P., et al. 2012, ApJS, 200, 12
Holoien, T. W.-S., Stanek, K. Z., Kochanek, C. S., et al. 2016, arXiv:1610.03061 [astro-ph.HE]
Humphreys, E. M. L., Reid, M. J., Moran, J. M., Greenhill, L. J., & Argon, A. L. 2013, ApJ, 775, 13
Jang, I. S., & Lee, M. G. 2014, ApJ, 792, 52
Jang, I. S., & Lee, M. G. 2015, ApJ, 807, 133
Johnston, K., Scowcroft, V., Madore, B., et al. 2013, SMASH: Spitzer Merger History and Shape of the Galactic Halo, Spitzer Proposal
Jones, R. V., Carney, B. W., & Fulbright, J. P. 1996, PASP, 108, 877
Jones, R. V., Carney, B. W., & Latham, D. W. 1988, ApJ, 332, 206
Kaluzny, J., Kubiak, M., Szymanski, M., et al. 1995, A&AS, 112, 407
Kollmeier, J. A., Szczygieł, D. M., Burns, C. R., et al. 2013, ApJ, 775, 57
Komatsu, E., Smith, K. M., Dunkley, J., et al. 2011, ApJS, 192, 18
Lee, M. G., Freedman, W. L., & Madore, B. F. 1993, ApJ, 417, 553
Lee, M. G., & Jang, I. S. 2012, ApJL, 760, L14
Lee, M. G., & Jang, I. S. 2013, ApJ, 773, 13
Liu, T., & Janes, K. A. 1989, ApJS, 69, 593
Longmore, A. J., Dixon, R., Skillen, I., Jameson, R. F., & Fernley, J. A. 1990, MNRAS, 247, 684
Longmore, A. J., Fernley, J. A., & Jameson, R. F. 1986, MNRAS, 220, 279
Luck, R. E., & Lambert, D. L. 2011, AJ, 142, 136
Mackey, A. D., & Gilmore, G. F. 2003, MNRAS, 345, 747
Mackey, A. D., & Gilmore, G. F. 2004, MNRAS, 352, 153
Madore, B. 2002, TRGB Distance to the Maser Galaxy NGC 4258, HST Proposal
Madore, B. F., & Freedman, W. L. 1995, AJ, 109, 1645
Madore, B. F., & Freedman, W. L. 2005, ApJ, 630, 1054
Madore, B. F., & Freedman, W. L. 2012, ApJ, 744, 132
Madore, B. F., Mager, V., & Freedman, W. L. 2009, ApJ, 690, 389
Mager, V. A., Madore, B. F., & Freedman, W. L. 2008, ApJ, 689, 721
Marconi, M., Coppola, G., Bono, G., et al. 2015, ApJ, 808, 50
Martínez-Vázquez, C. E., Monelli, M., Bono, G., et al. 2015, MNRAS, 454, 1509
McConnachie, A. W. 2012, AJ, 144, 4
Méndez, B., Davis, M., Moustakas, J., et al. 2002, AJ, 124, 213
Michalik, D., Lindegren, L., & Hobbs, D. 2015, A&A, 574, A115
Mignard, F. 2003, in ASP Conf. Ser. 298, GAIA Spectroscopy: Science and Technology, ed. U. Munari (San Francisco, CA: ASP), 25
Mignard, F. 2005, in ESA Special Publication 576, The Three-Dimensional Universe with Gaia, ed. C. Turon, K. S. O'Flaherty, & M. A. C. Perryman 5
Minniti, D., Lucas, P. W., Emerson, J. P., et al. 2010, NewA, 15, 433
Monson, A. J., Freedman, W. L., Madore, B. F., et al. 2012, ApJ, 759, 146
Moretti, M. I., Clementini, G., Muraveva, T., et al. 2014, MNRAS, 437, 2702
Muraveva, T., Palmer, M., Clementini, G., et al. 2015, ApJ, 807, 127
Navarrete, C., Contreras Ramos, R., Catelan, M., et al. 2015, A&A, 577, A99
Neeley, J. R., Marengo, M., Bono, G., et al. 2015, ApJ, 808, 11
Perryman, M. A. C., Lindegren, L., Kovalevsky, J., et al. 1997, A&A, 323, L49
Persson, S. E., Madore, B. F., Krzemiński, W., et al. 2004, AJ, 128, 2239
Persson, S. E., Murphy, D. C., Smee, S., et al. 2013, PASP, 125, 654
Phillips, M. M. 2012, PASA, 29, 434
Pietrzyński, G., Graczyk, D., Gieren, W., et al. 2013, Natur, 495, 76
Planck Collaboration, Ade, P. A. R., Aghanim, N., et al. 2011, A&A, 536, A1
Planck Collaboration, Ade, P. A. R., Aghanim, N., et al. 2014, A&A, 571, A16
Planck Collaboration, Ade, P. A. R., Aghanim, N., et al. 2016, A&A, 594A, 13P
Rest, A., Scolnic, D., Foley, R. J., et al. 2014, ApJ, 795, 44
Rey, S.-C., Lee, Y.-W., Joo, J.-M., Walker, A., & Baird, S. 2000, AJ, 119, 1824
Riess, A. G., & Macri, L. 2007, BAAS, 39, 826
Riess, A. G., Macri, L., Casertano, S., et al. 2009, ApJ, 699, 539
Riess, A. G., Macri, L., Casertano, S., et al. 2011, ApJ, 730, 119
Riess, A. G., Macri, L. M., Hoffmann, S. L., et al. 2016, ApJ, 826, 56R
Rigault, M., Aldering, G., Kowalski, M., et al. 2015, ApJ, 802, 20
Rizzi, L., Tully, R. B., Makarov, D., et al. 2007, ApJ, 661, 815
Romaniello, M., Primas, F., Mottini, M., et al. 2005, A&A, 429, L37
Romaniello, M., Primas, F., Mottini, M., et al. 2008, A&A, 488, 731

Saha, A., Sandage, A., Tammann, G. A., et al. 2001, ApJ, 562, 314
Sakai, S., Ferrarese, L., Kennicutt, R. C., Jr., & Saha, A. 2004, ApJ, 608, 42
Salaris, M., & Cassisi, S. 1997, MNRAS, 289, 406
Salaris, M., Cassisi, S., & Weiss, A. 2002, PASP, 114, 375
Sandage, A., Beaton, R. L., & Majewski, S. R. 2016, PASP, 128, 064202
Sandage, A., Tammann, G. A., Saha, A., et al. 2006, ApJ, 653, 843
Sarajedini, A., Barker, M. K., Geisler, D., Harding, P., & Schommer, R. 2006, AJ, 132, 1361
Sarajedini, A., Mancone, C. L., Lauer, T. R., et al. 2009, AJ, 138, 184
Saviane, I., Hibbard, J. E., & Rich, R. M. 2004, AJ, 127, 660
Saviane, I., Momany, Y., da Costa, G. S., Rich, R. M., & Hibbard, J. E. 2008, ApJ, 678, 179
Schweizer, F., Burns, C. R., Madore, B. F., et al. 2008, AJ, 136, 1482
Scowcroft, V., Freedman, W. L., Madore, B. F., et al. 2011, ApJ, 743, 76
Scowcroft, V., Seibert, M., Freedman, W. L., et al. 2016, MNRAS, 549, 1170
Shappee, B., Prieto, J., Stanek, K. Z., et al. 2014, All Sky Automated Survey for SuperNovae (ASAS-SN or "Assassin"), in American Astronomical Society Meeting Abstracts 223, 236.03
Shappee, B. J., & Stanek, K. Z. 2011, ApJ, 733, 124
Skillen, I., Fernley, J. A., Stobie, R. S., & Jameson, R. F. 1993, MNRAS, 265, 301
Skrutskie, M. F., Cutri, R. M., Stiening, R., et al. 2006, AJ, 131, 1163
Smith, H. A. 1995, CAS, 27
Sollima, A., Cacciari, C., Arkharov, A. A. H., et al. 2008, MNRAS, 384, 1583
Sollima, A., Cacciari, C., & Valenti, E. 2006, MNRAS, 372, 1675
Spergel, D. N., Bean, R., Doré, O., et al. 2007, ApJS, 170, 377
Spergel, D. N., Flauger, R., & Hložek, R. 2015, PhRvD, 91, 023518
Spergel, D. N., Verde, L., Peiris, H. V., et al. 2003, ApJS, 148, 175
Stritzinger, M. D., Phillips, M. M., Boldt, L. N., et al. 2011, AJ, 142, 156
Sullivan, M., Conley, A., Howell, D. A., et al. 2010, MNRAS, 406, 782
Tabur, V., Kiss, L. L., & Bedding, T. R. 2009, ApJL, 703, L72
Trager, S. C., King, I. R., & Djorgovski, S. 1995, AJ, 109, 218
Turon, C., Luri, X., & Masana, E. 2012, Ap&SS, 341, 15
Walker, A. R. 1992, AJ, 103, 1166
Yang, S.-C., & Sarajedini, A. 2012, MNRAS, 419, 1362